IEEE Open Journal of the
Industrial Electronics Society

Received 7 May 2021; accepted 2 June 2021. Date of publication 8 June 2021;
date of current version 23 June 2021.

Digital Object Identifier 10.1109/OJIES.2021.3087418

Performance Evaluation of Modulation Techniques in Single-Phase Dual Active Bridge Converters

N. NOROOZI [1] (Member, IEEE), A. EMADI [1] (Fellow, IEEE), AND M. NARIMANI [1] (Senior Member, IEEE)

[1]Department of Electrical and Computer Engineering, McMaster University, Hamilton, ON L8S 4L8, Canada

CORRESPONDING AUTHOR: N. NOROOZI (e-mail: noroozin@ mcmaster.ca).

ABSTRACT This research presents a thorough comparison of different modulation techniques employed in dual active bridge (DAB) converters. The performance of a DAB converter is essentially affected by the modulation technique and the operating point, including power level, input, and output voltages. A deep understanding of different modulations is required to achieve the highest performance in the entire operating range. Therefore, this paper focuses on comparing different modulation techniques over a DAB converter's operating span. The comparison results provide guidance to apply the correct modulation in certain working areas keeping the converter on top of its performance. Moreover, the paper proposes an optimization solution with distinct objective functions adoptable in DAB converters to reduce power loss. The proposed optimization approach outperforms the existing solutions regarding generality and simplicity. The optimization associates with the modulation techniques that include more than one degree of freedom, such as extended phase shift (EPS) and dual-phase shift (DPS). The proposed optimization and the investigated modulation techniques are evaluated in terms of the converter's efficiency, current stress, and backflow power. The evaluation is realized by the simulation study of a 10 kW 800V/500V SiC-based DAB converter in PLECS software.

INDEX TERMS Dual active bridge (DAB) converter, efficiency, modulation techniques, backflow power, current stress.

I. INTRODUCTION

The Utilization of a DAB converter in DC-DC conversion offers remarkable advantages such as bidirectional power transfer, high power density, high efficiency, the simple realization of soft switching, and galvanic isolation [1], [2]. Thanks to the supremacies of a DAB converter, the topology is exploited in various industries, including automotive, aerospace and, sustainable energy systems [3]–[6]. The DAB converters are also rewarding in high-voltage and high-power applications, where they are used as core cells in cascade or parallel structures [7]–[9].

The main structure of a single-phase DAB converter is illustrated in Fig. 1. The basic modulation technique of a DAB is called single-phase shift (SPS) modulation, in which, each bridge receives 50% diagonal gate pulses. The phase shift between the two bridges is regulated based on the required power. By using SPS, v_{t1} and v_{t2} in Fig. 1 appear as two-level square waves [10].

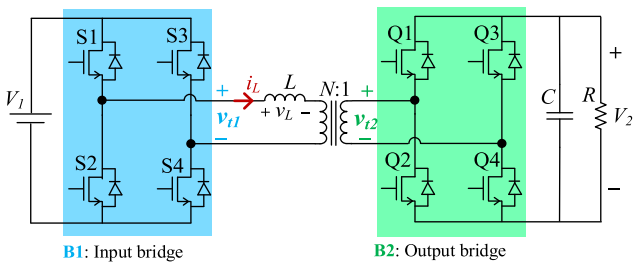

FIG. 1. The main structure of a single-phase DAB converter.

Despite the outstanding features, a DAB converter discloses drawbacks as well. One major issue with a DAB converter

is that its performance varies over its operating range. It is worth noting, a DAB's performance deteriorates significantly in lower power ratios [11]. Furthermore, zero-voltage switching (ZVS) in an SPS-modulated DAB converter is solely attainable in a limited working area, and due to the high-switching loss, the system efficiency declines dramatically out of the ZVS zones.

Many alternative modulation methods have been proposed in recent literature to overcome the shortages of SPS. For example, a "PWM modulation technique" is proposed in [12], [13], in which a three-level pulse-width-modulated voltage drives the bridge with the higher equivalent voltage. This technique improves the specification of the DAB converter in terms of current RMS and peak values, and the total efficiency [14], [15]. The extended phase shift (EPS) modulation is presented in [16]–[19] that offers the expansion of the ZVS zone and the reduction of the backflow power (BFP) and current stress. Additionally, EPS can be associated with optimization algorithms to enhance the overall performance, owing to two degrees of freedom [20], [21].

Dual-phase shift (DPS) modulation is presented in [22]–[25] that employs PWM voltages for both bridges. The DPS method is accompanied by some optimization methods in [26], [27] targeting the reduction of BFP and current stress. DPS enhances the total performance of a DAB converter compared to SPS, mainly in medium and light loads. However, complex math calculations are required to exploit the benefits of one more degree of freedom utilizable in DPS.

The triple-phase-shift modulation technique (TPS) offers further flexibility, compared to EPS and DPS, thanks to three degrees of freedom, [28], [29]. In the TPS method, the phase shift and the duty cycles of v_{t1} and v_{t2} are adjusted based on particular objectives. For example, TPS is used to minimize the current stress in [20] and [30], and BFP in [31]. Despite the satisfying results, the optimization of the three parameters demands massive numerical calculation and effortful implementation.

Triangular modulation (TRG) presented in [32]–[34] has the supremacy of the lowest switching loss among all the existing modulation techniques. The appellation is originated from the triangular shape of the leakage inductor current (i_L in Fig. 1) produced by employing this modulation method. The TRG method features soft switching in all turn-on moments and zero-current switching (ZCS) for six turn-off instants. However, TRG has some drawbacks, namely, the low capability of power transfer and high reactive power.

The basic of the trapezoidal modulation (TRP) resembles that in TRG. In addition to soft-switched turn-on in all switches, ZCS is also realized in four switches at turn-off moments. The transferable power range using TRP covers the median power ratios [11]. A comparison of TRP and SPS in [35] concludes the excellence of SPS if MOSFET switches are used. In [36], TRP is slightly modified by a fixed duty cycle. compensation, targeting efficiency improvement. However, this modification is case-dependent, and the efficiency enhancement is not significant.

The combinational modulation technique (CC) is investigated in [34] and [37], [38], seeking a higher efficiency. The strategy utilizes distinct modulation approaches in different operation zones. In [34], TRG is applied at light loads, while the system's major modulation technique is SPS. Similarly, in [37] TRG, EPS, and SPS are used to transfer the power in small, medium, and large ratios, respectively. The method in [37] brings about loss reduction, and consequently higher efficiency. Due to the parameter adjustment and the boundaries determination, the approach requires massive numerical calculations.

As discussed, the modulation techniques play a significant role in forming the DAB's specification over the operating range. Besides, there are various modulation techniques that can be enhanced by different optimization objectives. Therefore, a thorough assessment of the existing modulation methods is vital to attain the DAB's highest potential performance. In [39], a general comparison of DPS, EPS, and SPS is presented, but the research lacks numerical results. Furthermore, many control methods are surveyed in [40], however, the evaluation is limited to the nominal power, and it considers a few approaches.

This study presents a detailed comparison of the existing modulation techniques in the full range of a DAB converter. This assessment is a guide to achieve the converter's highest performance by selecting the most efficient modulation at that time. Moreover, the paper proposes a generalized optimization approach associates with EPS and DPS. DAB converters' power equations and the working constraints are converted to a standard form of a nonlinear optimization problem solvable by a common solver such as MATLAB. Following a detailed clarification of the existing modulation techniques, these modulations and the proposed optimization are assessed in terms of the converter's efficiency, current stress, and backflow power over the full operating range. The simulation results obtained from the PLECS software prove the accuracy of the proposed optimization solution.

The paper is organized as follows: the DAB converter principle and the SPS control are discussed in Section II. The alternative control methods are clarified in Section III. The proposed optimization approach is elaborated in Section IV. The results obtained from the evaluation of different modulation technique are presented in Section V. Finally, the conclusion of the study is expressed in Section VI.

II. OPERATION OF A DUAL ACTIVE BRIDGE CONVERTER

The high-frequency power transmission in a DAB converter primarily resembles the power flow in a sinusoidal power system depicted in a simplified form in Fig. 2(a). The transmitted power in Fig. 2(a) is equal to (1), [39]:

$$P = \frac{V_{rms1} V_{rms2}}{2\pi f L} \sin(\varphi) \tag{1}$$

where V_{rms1} and V_{rms2} are the RMS values of the voltage sources; f is the main frequency of the sources; and φ is the phase shift between the sources. If the sinusoidal sources are

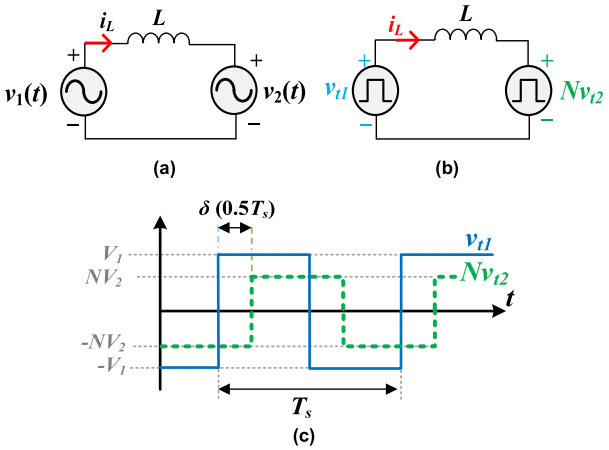

FIG. 2. Power transmission between two voltage sources. (a) The traditional sinusoidal system, (b) the simplified equivalent circuit of ta DAB converter, (c) the 50% bipolar pulsating voltages.

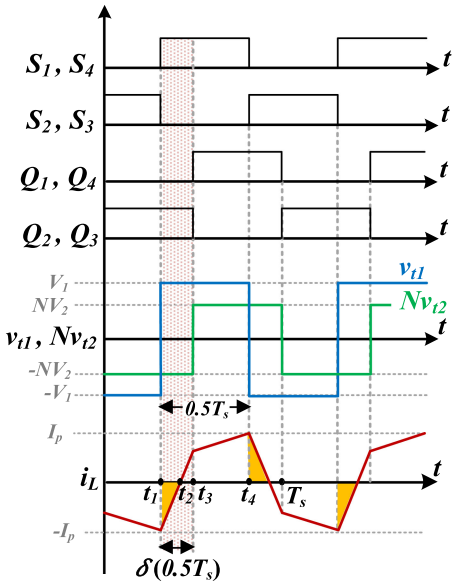

FIG. 3. Typical waveforms of the gate signals, v_{t1}, Nv_{t2} and i_L in SPS.

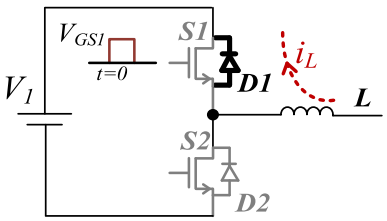

FIG. 4. The visual clarification of ZVS at S1's turn-on moment.

replaced with pulsating voltage sources, the power transmission takes place in a similar manner. Fig. 2(b), (c) illustrate the equivalent circuit of a DAB converter and the voltages waveform. L in Fig. 2(b), (c) denotes the transformer's leakage inductor. Assuming bipolar 50% pulsating sources for v_{t1} and Nv_{t2} with peak values of V_1 and NV_2, respectively, the DAB's power can be calculated as, :

$$P = \frac{NV_2V_1}{2\pi^2 Lf_s}\varphi\,(\pi - |\varphi|) \tag{2}$$

where f_s and φ are the switching frequency and the phase shift between the two high-frequency sources. In the following, the DAB operation is studied in detail:

A. SINGLE-PHASE SHIFT CONTROL

The single-phase shift (SPS) modulation is the most basic control of a DAB converter, in which the bridges are driven by 50% pulses. Fig. 3 displays the gate signals (S_i and Q_i, $i = 1, .., 4$), the leakage current (i_L), and the transformer's equivalent voltages (v_{t1}, Nv_{t2}) using SPS. The phase shift between v_{t1} and v_{t2} is defined by δ pointed in Fig. 3. The power transmitted in the positive direction is calculated as [16]:

$$P = \frac{1}{T_s}\int_0^{T_s} v_{t1}i_L dt = \frac{2}{T_s}V_1\int_0^{0.5T_s} i_L\,dt \tag{3}$$

Considering Fig. 3, $i_L(t)$ values at the moments of $t_1, \ldots, t_4$ are expressed as:

$$\begin{cases} i_L\,(t_1) = -I_p \\ i_L\,(t_2) = 0 \\ i_L\,(t_3) = i_L\,(t_1) + \frac{V_1+NV_2}{L}\left(\frac{\delta T_s}{2}\right) \\ i_L\,(t_4) = i_L\,(t_3) + \frac{V_1-NV_2}{L}\left(\frac{(1-\delta)T_s}{2}\right) = I_p \end{cases} \tag{4}$$

By using (4) in (3), the transmitted power and the peak current value are calculated as, [2]:

$$I_{P,SPS} = \frac{V_1 - NV_2\,(1-2\delta)}{4Lf_s} \tag{5}$$

$$P_{SPS} = \frac{NV_2V_1}{2Lf_s}\delta\,(1-\delta) \tag{6}$$

The power's peak value in SPS is defined by $P_{max,SPS}$, where:

$$P_{max,SPS} = \frac{NV_1V_2}{8Lf_s} \tag{7}$$

It is also worth mentioning that there is an odd symmetry to transmit the power in the opposite direction (negative power), [39].

B. ZERO-VOLTAGE SWITCHING ZONES

The SPS control provides the converter with ZVS at turn-on moments of the switches [41]. However, the ZVS feature discontinues in some parts of the operating area. Particularly, at light loads, most of the operation area is excluded from the ZVS zone. Fig. 4 describes an example of the ZVS realization at turn-on moments of the switches in a DAB converter. For

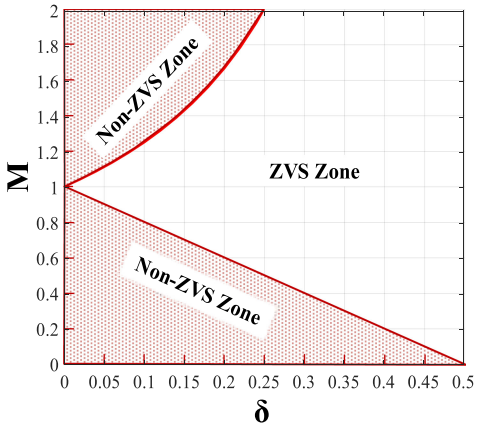

FIG. 5. The ZVS and non-ZVS zones associated with M and δ, $M = NV_2/N_1$..

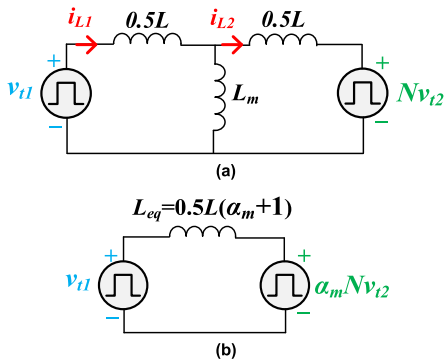

FIG. 6. The transformer of a DAB, considering the magnetizing inductance, (a) T-model of the transformer, along with the pulsating voltage sources, (b) the simplified model.

example, if D_1 conducts when the corresponding gate signal is received, the switching action is carried out under nearly zero-voltage. In other words, the polarity of i_L at the turn-on moments determines if ZVS is obtainable or not. The turn-on ZVS constraints regarding the inductor current's polarity are summarized as (8), [30]:

$$\begin{cases} S_1,\ S_4,\ Q_2,\ Q_3\ at\ \ i_L < 0 \\ S_2,\ S_3,\ Q_1,\ Q_4\ \ at\ \ i_L > 0 \end{cases} \tag{8}$$

The spotted area in Fig. 5 indicates the non-ZVS zone on the (δ, M) surface using SPS, where M is the voltage ratio equal to NV_2/V_1 and δ is the phase shifting angle. Notably, ZVS is feasible surrounding the central line, even at light loads (small values of δ). The ZVS constraints in (8) deduce the inequalities that represent the ZVS zone:

$$\begin{cases} \delta > \frac{M-1}{2M}, & M > 1 \\ \delta > \frac{1-M}{2}, & M < 1 \end{cases} \tag{9}$$

The accuracy of the ZVS constraints is upgraded by involving the magnetizing inductor [42], and the switches' detailed characteristics [43]. The analysis concerning the ZVS boundaries is also improved in [41], by taking the switches' parasitic capacitance into account:

$$\begin{cases} \delta > \frac{M-1}{2M} + 4f_s\sqrt{LC_{eq1}}, & M > 1 \\ \delta > \frac{1-M}{2} + \frac{4f_sM}{n}\sqrt{LC_{eq2}}, & M < 1 \end{cases} \tag{10}$$

In practice, a safety margin should be considered in the design procedure to avoid entering the non-ZVS-Zone.

C. THE EFFECT OF MAGNETIZING INDUCTANCE

The transformer T-model is utilized to investigate the magnetizing inductance effect on power transmission in a DAB converter, as depicted in Fig. 6(a) [42]. The T-model is simplified to the circuit in Fig. 6(b), using the primary circuit rules, where [42]:

$$\begin{cases} L_{eq} = \frac{L}{2} + \frac{0.5L\times L_m}{0.5L+L_m} = \frac{L(1+\alpha_m)}{2} \\ \alpha_m = \frac{1}{1+0.5L/L_m} \end{cases} \tag{11}$$

Therefore:

$$P_{SPS} = \frac{NV_2V_1}{2Lf_s}\delta(1-\delta)\left(\frac{2\alpha_m}{1+\alpha_m}\right) \tag{12}$$

Comparing (12) and (6) concludes that the magnetizing inductor reduces the maximum power to some extent. Since L/L_m is normally small, α_m can be approximated to 1. Therefore, it is safe to argue that the magnetizing inductor effect is usually insignificant in the DAB analysis [42].

The ZVS boundaries are also affected slightly by the magnetizing inductance. By obtaining i_{L1} and i_{L2} from the circuit equations in Fig. 6(a), the ZVS conditions are modified as:

$$\begin{cases} \delta > \frac{\alpha_m M-1}{2\alpha_m M}, & M > \frac{1}{\alpha_m} \\ \delta > \frac{1-\alpha_m M}{2}, & M < \frac{1}{\alpha_m} \end{cases} \tag{13}$$

The coefficient, α_m, moves the ZVS boundaries. However, this replacement is normally inconsiderable.

D. BACKFLOW POWER (BPF)

BFP in a DAB converter refers to the power flow in the reverse direction that occurs in a portion of a switching cycle. BFP brings about some adverse consequences, such as increasing loss and current stress. The filled triangles in Fig. 3 represent the backflow areas, where the polarity of v_{t1} and i_L are opposite. The BPF in the SPS control ($P_{BFP,SPS}$) is calculated according (14), [21]:

$$P_{BFP,SPS} = \frac{1}{0.5T_s}\int_{t_1}^{t_2} v_{t1}\times i_L dt \tag{14}$$

By replacing the related parameters in (8), it is concluded that:

$$P_{BFP,SPS} = \begin{cases} \frac{[k+(2\delta-1)]^2}{2(k+1)}, & NV_2 \le V_1 \\ \frac{[M+(2\delta-1)]^2}{2(M+1)}, & NV_2 > V_1 \end{cases} \quad (15)$$

where:

$$K = \frac{1}{M} = \frac{V_1}{NV_2} \quad (16)$$

The term of BPF is misnamed in some previous works, where they call it "the reactive power." Indeed, BPF is only a portion of the reactive power (Q), based on the primary definitions in an electrical system. It is notable that the instantaneous power excluding the BFP area contains some extra harmonic components that are not associated with the active power transfer.

E. DESIGN PROSEDURE FOR A DAB CONVERTER

A simple design procedure is suggested in this paper, which is organized into four steps:

1) SPECIFYING THE TRANSFORMER RATIO

Typically, N is selected to locate the nominal voltage range at the central line, where $V_1 = NV_2$.

2) IDENTIFYING THE PHASE SHIFT SPAN

The design strategies for δ_{max} determination ($\delta \in (\delta_{min}, \delta_{max})$) are categorized into two groups, aiming at 1) higher efficiency, and 2) more extended ZVS zone, [41]. Higher δ_{max} results in a larger L, a wider ZVS zone, and a more flattened efficiency curve. In contrary, lower δ_{max} gains higher efficiency peak with restricted ZVS area. In [41] the two schemes are compared by setting δ_{max} to 0.04 and 0.35. It is worth mentioning the control loop degrades by significant nonlinearity if δ_{max} is selected higher than 0.4. The lower boundary of δ_{max} is calculated by using (9), with regards to the voltage range.

Due to the switches' rise and fall time, the DAB converter malfunctions if a minimal phase shift is applied. Therefore, in practice, there is a restriction for the minimum operating power in a DAB converter. In [34], a modified TRG is proposed to expand the power range from its lower boundary.

3) DESIGN OF L

The inductor value (L) is designed using (17) and the second step.

$$L < \frac{NV_2V_1}{2P_{max}f_s}\delta_{max}\,(1-\delta_{max}) \quad (17)$$

An external inductor can be connected in series with the DAB's transformer to achieve the required inductance for the power transmission [44].

4) VERIFICATION OF THE ZVS CONSTRAINTS

If the inequalities in (10) are unsatisfied, a larger value of δ_{max} should be considered. The proposed simple design procedure is summarized in Fig. 7. However, there are many more considerations in a practical design, including the semiconductor components selection and the magnetic design. The loss model of a DAB converter in [1] and [44], [45] can be considered in a more accurate design procedure. Moreover, the switching deadtime adjustment in [46], [48] can be employed.

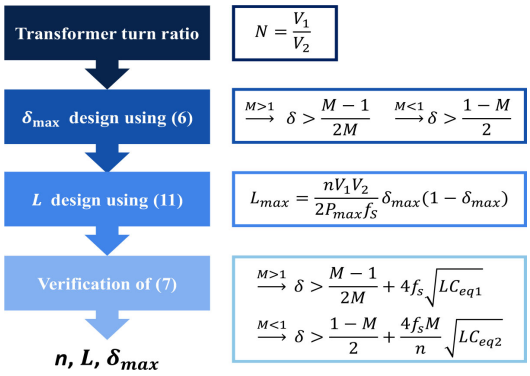

FIG. 7. A simple design procedure for a DAB converter.

F. CLOSED-LOOP CONTROLLER DESIGN

The design and implementation of a proper closed-loop controller in the DAB converter require precise small-signal analysis [49]. In [50], the DAB converter function is modeled by four hypothetical parallel DABs controlled by SPS. The DAB's steady-state and small-signal characteristic is approximated using the first switching harmonic of the current and voltage. The model is rather simple and practical. A more precise approach is explained in [51], which proposes a modeling framework. The model represents the DAB's primary equations. However, the model entails a much higher complexity compared to [50].

All the DAB modulation techniques, such as SPS, EPS, etc. are covered by the generic models in [50], [51]. The controller can be realized by the traditional voltage loop in [23] and [52]. More sophisticated schemes are also proposed in the literature, including, predictive current mode controller [53], nonlinear disturbance observer [54], and sliding-mode controller [55]. Adding an inner current control loop improves the dynamic response of the converter and simplifies the overcurrent protection, [53]. However, the dual-loop techniques based on PI can provide a narrow operating bandwidth. Load-current feed-forward approaches in [56] and [54] are proposed as a solution for the limited bandwidth. The direct power control scheme in [57] is also recommended to enhance the controller's robustness.

III. ALTERNATIVE MODULATION TECHNIQUES

Due to the shortages of SPS—including limited ZVS zone, inferior performance at low power ratios, high current stress, and a large portion of backflow power—alternative techniques have been developed to mitigate these deficiencies. In this section, the principle of the existing modulations is discussed.

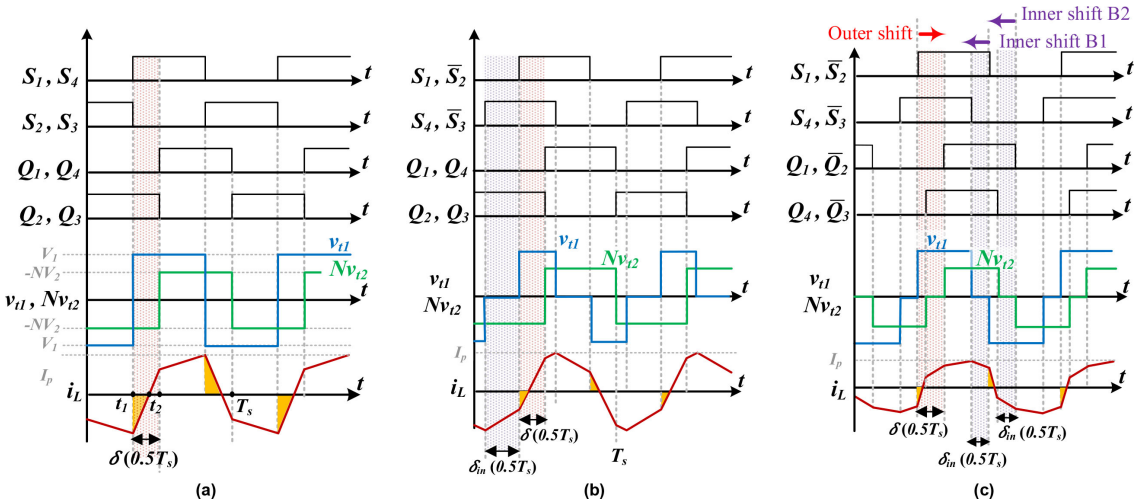

FIG. 8. Typical waveforms of v_{t1}, Nv_{t2}, i_L and the gate signals ($0 \le \delta_{in} \le 1$) (a) the SPS modulation, (b) the EPS modulation, (c) the DPS modulation.

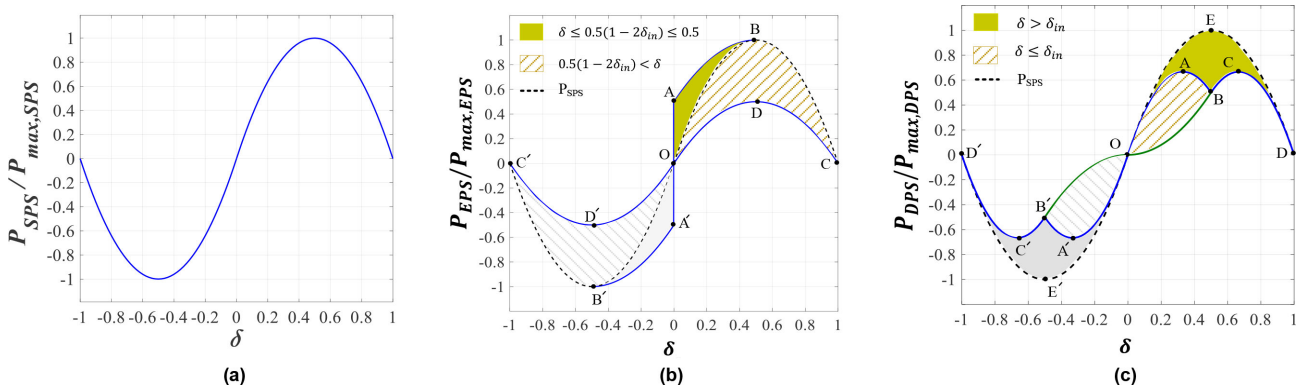

FIG. 9. The power characterization of the EPS control. (a) the SPS modulation, (b) the EPS modulation, (c) the DPS modulation.

A. EXTENDED PHASE SHIFT MODULATION (EPS)

The EPS modulation provides the converter with a wider ZVS zone, less BFP, and lower current stress compared to SPS, especially in medium power level [14]–[16]. The minimization of current peak and BPF can also be accomplished using optimization algorithms [58], [59]. Nevertheless, the SPS control can surpass EPS at the nominal power level in a wide voltage range DAB converter [37].

Unlike the SPS control, v_{t1} and v_{t2} contain three voltage levels using the EPS method. Fig. 8(b) illustrates the typical waveforms of v_{t1}, Nv_{t2}, i_L, and the gate signals in the EPS modulation, where δ_{in} denotes the relative inner phase shift. δ_{in} refers to the phase difference between the gate signals of two legs in the same bridge. It is worth noticing that δ_{in} is usually employed in the bridge with a larger equivalent voltage. For instance, if NV_2 is larger than V_1, then the inner shift is placed in the gate signals of B2. The point is comprehended if the loss analysis is considered, [37].

In the SPS control, S_1 should lead Q_1 to transmit the power in the positive direction. In contrary to SPS, S_1can lead or lag Q_1 for the power transfer from B1(input bridge) to B2 (output bridge) in EPS. As discussed in [21], the former stance (S_1 leading Q_1) outperforms the later if the positive power flow is intended.

The backflow power (BFP) regions and I_P level in EPS are highlighted in Fig. 8(b) by the filled areas and the dashed line, respectively. The comparison of Fig. 8(b) and Fig. 8(a), demonstrates that the BFP is reduced by replacing the traditional SPS method with EPS. Assuming S_1 leads Q_1, the power equation in the EPS approach equals:

$$P_{EPS} = \frac{NV_2V_1}{4Lf_s}\left[\delta_{in}\left(1-\delta_{in}-2\delta\right)+2\delta\left(1-\delta\right)\right] \tag{18}$$

The power transfer characterization of the EPS control is illustrated in Fig. 9(b), where the dashed line represents P_{SPS}. The maximum transferable power in EPS is equal to that in SPS [21]:

$$P_{max,\,EPS} = P_{max,\,SPS} \tag{19}$$

TABLE I Power, BFP and Current Stress Equations in SPS, EPS and DPS

Variable	EPS	EPS	DPS
P_{max}	$\frac{NV_2V_1}{8Lf_s}$	$\frac{NV_2V_1}{8Lf_s}$	$\frac{NV_2V_1}{8Lf_s}$
P/P_{max}	$4\delta(\delta-1)$	$[2\delta_{in}(1-2\delta-\delta_{in})+4\delta(\delta-1)]$	$\delta \geq \delta_{in}$ $[-2\delta_{in}^2+4\delta(1-\delta)]$ $\delta < \delta_{in}$ $\delta[4-4\delta_{in}-2\delta]$
$P_{BFP}/P_{max}, NV_2 \leq V_1$	$\frac{[k+(2\delta-1)]^2}{2(k+1)}$	$\frac{[k(1-\delta_{in})+(2\delta-1)]^2}{2(k+1)}$	$\frac{[k(1-\delta_{in})+(2\delta-1-\delta_{in})]^2}{2(k+1)}$
$P_{BFP}/P_{max}, NV_2 > V_1$	$\frac{[M+(2\delta-1)]^2}{2(M+1)}$	$\frac{[M(1-\delta_{in})+(2\delta-1)]^2}{2(M+1)}$	$\frac{[M(1-\delta_{in})+(2\delta-1-\delta_{in})]^2}{2(M+1)}$
$I_p, NV_2 \leq V_1$	$\frac{V_1-NV_2(1-2\delta)}{4Lf_s}$	$\frac{1}{4Lf_s}[V_1(1-\delta_{in})-NV_2(1-2\delta-2\delta_{in})]$	$\frac{1}{4Lf_s}[V_1(1-\delta_{in})-NV_2(1-2\delta-\delta_{in})]$
$I_p, NV_2 > V_1$	$\frac{NV_2-V_1(1-2\delta)}{4Lf_s}$	$\frac{1}{4Lf_s}[NV_2(1-\delta_{in})-V_1(1-2\delta-2\delta_{in})]$	$\frac{1}{4Lf_s}[NV_2(1-\delta_{in})-V_1(1-2\delta-\delta_{in})]$

The upper and lower boundaries of the transmission power in Fig. 9(b) are marked by the letters A, B, C, D and O in the positive power region (right side of the curve). The equations describing these boundaries are summarized as, [16]:

$$\begin{cases} AB: \ \delta_i = 0.5\,(1-2\delta)\,, \quad \delta \leq 0.5 \\ BC: \ \delta_i = 0, \delta > 0.5 \\ ODC: \ \delta_i = 1-\delta \end{cases} \tag{20}$$

The inequalities indicated in (21), (22) are satisfied in the filled and hatched areas of Fig. 9(b), respectively:

$$\delta \leq 0.5\,(1-\delta_{in}) \leq 0.5 \tag{21}$$

$$0.5\,(1-\delta_{in}) \leq \delta \tag{22}$$

The tracking of the power curve upper boundary in the EPS control ($A \rightarrow B$ in Fig. 9(b)) is used as a core to adjust δ_{in} and δ values in [16]. The comparison between SPS and EPS in [16] reveals that EPS reduces the BFP and I_p.

As pointed before, δ_{in} and δ can also be adjusted using optimization processes to minimize I_p and BFP. However, the optimization techniques demand a vast amount of math calculation, which brings about high complexity. The ZVS constraints of the EPS control are also considered as a part of the optimization process. The constraints are clarified in [12], [13].

Table I summarizes the parametric values of BFP, I_p , and the power in the EPS control, [20], [21]. Similar to that presented control in (3), (4) concerning SPS, the equations in Table I can be calculated using the current and voltage waveforms. It is worth noting that there is an odd symmetry in the power transmission curve. It means that to transfer the power in the reverse direction (the left side of Fig. 9(b)), $-\delta$ and $-\delta_{in}$ are replaced with δ and δ_{in} in all the positive direction's equalities and inequalities. In this case, the power's polarity will be negative, showing the odd symmetry in the curve.

B. DUAL PHASE SHIFT MODULATION (DPS)

Another alternative modulation technique is DPS, which resembles the EPS approach. The main difference is related to the inner phase shift, which is assigned equally to both bridges, instead of one, [22] and [60]. The approach is applied to a current-fed DAB in [61], pursuing higher efficiency in light loads, through the expansion of the ZVS zone. Similarly, the DPS control is used in [62], to attain the minimum loss in the converter, using a rather intricate optimization process. Fig. 8(c) illustrates the typical waveforms of i_L, v_{t1}, Nv_{t2}, and the corresponding gate signals. The BFP regions and I_p level are also highlighted in Fig. 8(c) by the filled triangles and the dashed line, respectively.

The power equation in the DPS modulation is expressed as, [25]:

$$P_{DPS} = \frac{NV_2V_1}{2Lf_s} \times \begin{cases} \left[-\frac{1}{2}\delta_{in}^2 + \delta\,(1-\delta)\right], & \delta \geq \delta_{in} \\ \delta\left[1-\delta_{in}-\frac{1}{2}\delta\right], & \delta < \delta_{in} \end{cases} \tag{23}$$

The maximum power in the DPS control is equal to that in the SPS method:

$$P_{max,DPS} = P_{max,SPS} \tag{24}$$

It is worth remarking to actualize the power transfer by the DPS control, δ and δ_{in} should satisfy (25) ([25] and [63]):

$$\delta + \delta_{in} < 1 \tag{25}$$

The transmission power area associated with the DPS control is depicted in Fig. 9(c), in which the upper and lower

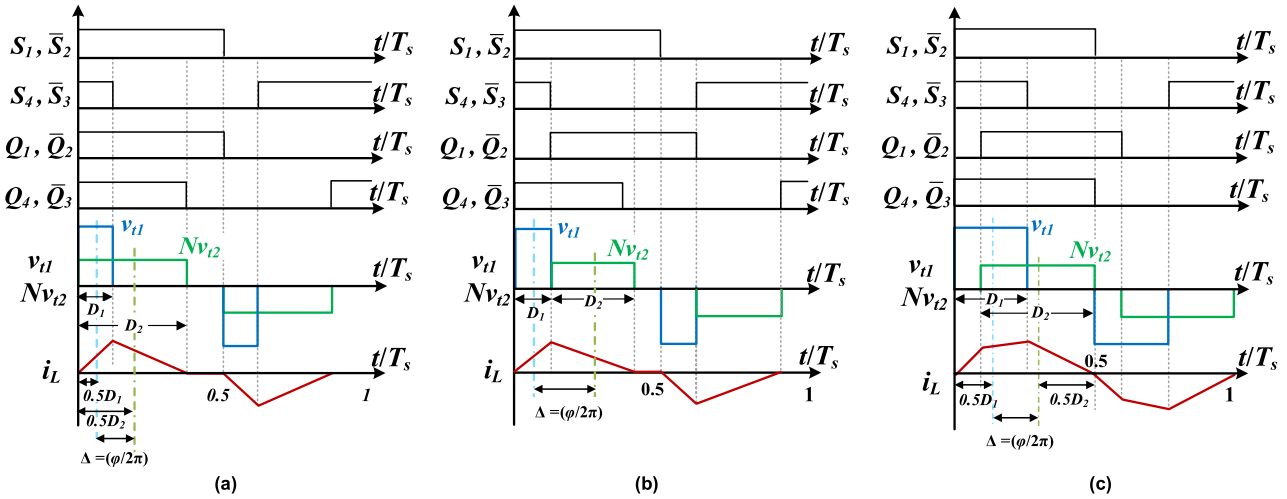

FIG. 10. Typical waveforms of v_{t1}, Nv_{t2}, i_L for $V_1 > NV_2$ and $P_{TRG} > 0$ in (a) TRG, (2) MTRG, (3) TRP.

power boundaries meet (26):

$$\begin{cases} OAB: & \delta_i = \delta, & \delta \le 0.5 \\ OB: & \delta_i = 1-\delta, & \delta \le 0.5 \\ BCD: & \delta_i = 1-\delta, & \delta > 0.5 \\ OED: & \delta_i = 0 \end{cases} \tag{26}$$

For $\delta \le 0.5$ and $\delta \le \delta_i$, the power transmission area is surrounded by the closed curve, $O \to A \to B$, in Fig. 9(c). This area is hatched on the right side of Fig. 9(c). Obviously, to transfer the power at the nominal level, the working point should be located outside of this area, depicted by the filled area in Fig. 9(c). In other words, for high power transmission, the phase shift should be larger than the inner phase shift ($\delta > \delta_{in}$). Moreover, Fig. 9(c) illustrates the validity of (25), considering that for $\delta + \delta_{in} > 1$, the working point is not located in power transmission areas.

The main equations in the DPS modulation are summarized in Table I ([25] and [62]). As explained in EPS, the odd symmetry in the power transmission curve is also valid in the DPS modulation. Similarly, by replacing $-\delta$ and $-\delta_{in}$ with δ and δ_{in}, the power transmission equations change to the negative direction.

In [64], the DPS modulation is modified targeting at the dynamic improvements, particularly at light loads. For this purpose, the direction of the inner shift in B1 is reversed. This modification changes the constraint in (25) to:

$$-\delta + 2\delta_{in} < 1 \tag{27}$$

In Fig. 8(c), the direction of the inner and outer phase shifts for the conventional DPS are pointed by the arrows at the top of the figure.

Compared to the traditional SPS, using DPS provides the DAB converter with performance improvement, especially at medium loads. However, the adjustment of the δ and δ_{in} requires some complex mathematical calculations.

C. TRIANGULAR MODULATION TECHNIQUE (TRG)

The TRG modulation introduced in [32] enables twelve ZCS and two ZVS transitions out of sixteen. Compared to the other approaches, ZCS provides the converter with the highest efficiency at lower power ratios. However, the power transmission area is limited in the TRG control, which means that TRG does not support a wide operating area. Indeed, TRG is more fitted to low power levels, owing to its high efficiency in that range, [11], [65]. TRG efficiency in medium power levels (for example, at 50% of nominal power) is rather low due to the significant value of disruptive harmonics in i_L.

The transformer's voltage and current waveforms in conventional TRG method are illustrated in Fig. 10(a) and Fig. 11(a) for $V_1 > NV_2$ and $V_1 < NV_2$, respectively, where D_1 and D_2 denote the duty cycle of v_{t1} and v_{t2}. The ZVS turn-on moments occur at the current peak value as shown in Fig. 10(a) and Fig. 11(a). During the other transitions, the current is zero, expressing the ZCS condition. φ in Fig. 10 and 11 represents the phase shift of v_{t1} and v_{t2}. In other words, φ is the phase distance between the midpoints of two voltage waveforms. Accordingly, Δ is specified as:

$$\Delta = \varphi/2\pi \tag{28}$$

The equations related to the TRG are indicated as:

$$\begin{cases} D_1 V_1 = NV_2 D_2 \\ \Delta = \varphi/2\pi = 0.5\,|D_2 - D_1| \\ P_{TRG} = \frac{\varphi^2 V_1 (NV_2)^2}{\pi^2 f_s L (V_1 - NV_2)}, V_1 > NV_2 \\ P_{TRG} = \frac{\varphi^2 (NV_2)(V_1)^2}{\pi^2 f_s L (NV_2 - V_1)}, \ V_1 < NV_2 \end{cases} \tag{29}$$

The maximum power transfer using the TRG control can be achieved when D_2 in Fig. 10(a) or D_1 in Fig. 11(a) is equal to $0.5T_s$. It means that the entire switching cycle is utilized to the power transfer. The maximum power in the TRG control

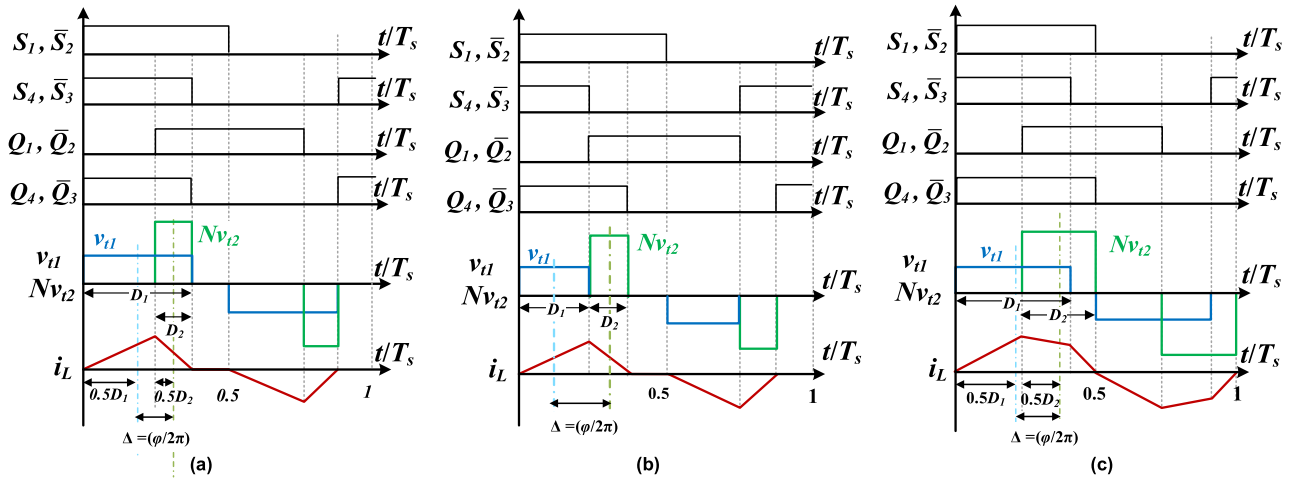

FIG. 11. Typical waveforms of v_{t1}, Nv_{t2}, i_L for $V_1 < NV_2$ and $P_{TRG} > 0$ in (a) TRG, (2) MTRG, (3) TRP.

is calculated as:

$$\begin{aligned} P_{max,TRG} &= \frac{(NV_2)^2(V_1-NV_2)}{4f_sLV_1}, V_1 > NV_2 \\ P_{max,TRG} &= \frac{(V_1)^2(NV_2-V_1)}{4f_sLNV_2}\ ,\ V_1 < NV_2 \end{aligned} \tag{30}$$

According to (30), the power transmission around the central line ($V_1 = NV_2$) is not feasible by the TRG control. In [34], a modified TRG is proposed to support the power transmission in the central line's vicinity. Fig. 10(b) and Fig. 11(b) illustrates v_{t1}, v_{t2}, and i_L using the modified TRG (MTRG), which actualizes eight ZCS (including turn-on and turn-off) and four ZVS (turn-on) out of sixteen transitions. Compared to the classic TRG, there are two extra hard-switched turn-off moments in MTRG, leading to higher loss. The power equations in MTRG are described as follows, [34]:

$$P_{MTRG} = \frac{D_1^2{V_1}^2}{f_sL} \tag{31}$$

$$P_{max,MTRG} = \frac{(NV_2)^2{V_1}^2}{4f_sLV_1\,(NV_2+V_1)} \tag{32}$$

This approach can be employed in the work points which are not supported by the TRG control. Notably, the efficiency in MTRG is low.

D. TRAPEZOIDAL MODULATION TECHNIQUE (TRP)

Despite the remarkable similarities between TRG and TRP, the power range and the number of soft-switched transitions are different in two techniques. TRP provides eight ZCS transitions and four ZVS turn-ons, out of the total sixteen. Four transitions are theoretically hard switching in TRP, meaning two more than that in TRG. When the entire switching period is utilized, TRP operates in the boundary condition, resulting in the highest performance of TRP, [36]. Fig. 10(c) and Fig. 11(c) depicts the typical waveforms of v_{t1}, v_{t2} and i_L in the marginal TRP. To realize the TRP modulation (33) should be satisfied:

$$\begin{cases} D_1V_1 = NV_2D_2 \\ \frac{\varphi}{2\pi} = 0.5\,(1-D_1-D_2) \end{cases} \tag{33}$$

The power equation ($P > 0$) and the maximum transmission power in TRP are described in (34), (35), respectively [33].

$$P_{TRP} = \frac{NV_1V_2\left[2NV_1V_2\left(\pi^2-2\varphi^2\right)-\left({V_1}^2+(NV_2)^2\right)(\pi-2\varphi)^2\right]}{4\pi^2f_sL(V_1+NV_2)^2} \tag{34}$$

$$\begin{cases} P_{TRP,max} = \frac{(NV_1V_2)^2}{4f_sL\left({V_1}^2+NV_1V_2+(NV_2)^2\right)} \\ \varphi_{TRP,max} = \frac{\pi}{2}\left(1-\frac{NV_1V_2}{{V_1}^2+NV_1V_2+(NV_2)^2}\right) \end{cases} \tag{35}$$

The power level in TRP is higher than in TRG, in the way that:

$$P_{max,TRG} < P_{TRP} \le P_{max,TRP} \tag{36}$$

In [35], a comprehensive comparison between TRP and SPS is made. Despite decreasing the switching loss, the efficiency declines in a TRP-modulated DAB with MOSFET switches [35]. The increase in the amount of undesired current harmonics in the TRP brings about a higher conduction loss. Oppositely, in a DAB with IGBT switches, the TRP overcomes SPS, particularly in lower power values. Table II, provides a summary of power equations in TRG, MTRG, and TRP.

E. COMBINATIONAL MODULATION TECHNIQUE

As mentioned, the performance of the modulation techniques varies over the operating range. In the combinational method, the applied modulation is coordinated on the power level, leading to a higher performance. In [34] and [37], [38], different modulation techniques are combined in a DAB converter,

TABLE II Power Equations in TRG, MTRG, and TRP

	TRG	MTRG	TRP
P	$\frac{\varphi^2 V_1 (NV_2)^2}{\pi^2 f_s L(V_1 - NV_2)}$, $V_1 > NV_2$ $\frac{\varphi^2 (NV_2)(V_1)^2}{\pi^2 f_s L(NV_2 - V_1)}$, $V_1 < NV_2$	$\frac{D_1^2 {V_1}^2}{f_s L}$	$\frac{NV_1V_2[2NV_1V_2(\pi^2 - 2\varphi^2) - ({V_1}^2 + (NV_2)^2)(\pi - 2\varphi)^2]}{4\pi^2 f_s L(V_1 + NV_2)^2}$
P_{max}	$\frac{(NV_2)^2(V_1 - NV_2)}{4f_s LV_1}$, $V_1 > NV_2$ $\frac{(V_1)^2(NV_2 - V_1)}{4f_s LNV_2}$, $V_1 < NV_2$	$\frac{(NV_2)^2 {V_1}^2}{4f_s LV_1(NV_2 + V_1)}$	$P_{TRP,max} = \frac{(NV_1V_2)^2}{4 f_s L({V_1}^2 + NV_1V_2 + (NV_2)^2)}$
Constraints	$D_1V_1 = NV_2D_2$ $\Delta = \varphi/2\pi = 0.5\lvert D_2 - D_1\rvert$	$D_1V_1 = NV_2D_2$	$D_1V_1 = NV_2D_2$, $\varphi = \pi(1 - D_1 - D_2)$ $P_{max,TRG} < P_{TRP} \leq P_{max,TRP}$

TABLE III Power Equations in TPS*

Mode	Condition	Power equation
I	$0 \leq \Delta \leq 0.5(D_2 - D_1)$	$\frac{NV_2V_1}{2Lf_s}\Delta D_1$
II	$0 \leq \Delta \leq 0.5(D_1 - D_2)$	$\frac{NV_2V_1}{2Lf_s}\Delta D_2$
III	$0.5\lvert D_1 - D_2\rvert \leq \Delta \leq \gamma$ **	$\frac{NV_2V_1}{16Lf_s}[2D_1D_2 + 4D_1\Delta - D_1^2 - D_2^2 - 4\Delta^2]$
IV	$0.5 - D_{av} \leq \Delta \leq D_{av}$ $D_{av} = 0.5(D_2 + D_1)$	$\frac{NV_2V_1}{8Lf_s}[4D_{av} + 4\Delta - D_1^2 - D_2^2 - 4\Delta^2 - 2]$
V	$D_{av} \leq \Delta \leq 0.5 - D_{av}$	$\frac{NV_2V_1}{4Lf_s}D_2D_1$

* The equations are presented in [30], [31] and [66]
** $\gamma = \min(D_{av}, (0.5 - D_{av}))$

covering the entire operating range. Typically, SPS and TRG are utilized at high and low power ratios, respectively. For example, in [34] the power range of an SPS-modulated DAB is expanded by using MTRG at lower power levels.

In addition to SPS and TRG, TPR in [38] and the optimized EPS in [37] are added to the DAB's control map at the medium power level. In [37], the boundaries between the middle and high-power levels are determined through intricate numerical calculations. Oppositely, the division lines in [38] are identified more simply. The control maps in [34] and [37], [38] are demonstrated in Fig. 12(a)–(c).

F. TRIPLE PHASE SHIFT MODULATION (TPS)

In the TPS method, optimization schemes are applied to obtain the optimal values for D_1, D_2 and φ, pursuing different objectives [30], [66]. The minimum RMS current in [67] and the expansion of ZVS zone in [66] are realized by the TPS control. The analysis in [30], [31] and [66] are based on the categorization of the current shape into different classes, specified in Table III. At the first stage of the optimization process, the optimal parameters are calculated separately for each category. Followingly, by comparison of the objective function values among all the current groups, the globally optimal values are acquired.

TPS with three degrees of freedom typically provides the converter with high performance. However, the calculation of the variables through optimization processes demands highly complex computation. The intricate optimization algorithms associating with the TPS technique reduces the functionality of the method significantly.

G. VARIABLE-FREQUENCY MODULATION TECHNIQUE

Generally, the main goal of alternative solutions is loss reduction, to obtain higher efficiency. The variable switching control is another strategy proposed in [68], [69] and [71], pursuing the same objective. In this approach, the switching frequency is regulated to expand the ZVS zone to cover a wider power span. Furthermore, a linear output power control can be attained by this scheme, [69]. Albeit the efficiency improvement, some deficiencies such as high voltage ripple and EMI problems emerge respectively at low and high switching frequencies in this method.

IV. THE PROPOSED OPTIMIZATION APPROACH

This section proposes a generalized offline optimization solution to determine optimal modulation parameters for EPS and DPS. Minimization of I_p and BFP are two distinct objectives of this optimization which are considered separately as target functions in this study. In contrast to the other optimization techniques in [20], [21], [26], [27], and [58], [59] which are confined to a specific modulation in a limited working area, the proposed optimization approach covers both EPS and DPS in the whole converter's operating range. In concise, it outperforms the existing optimization techniques regarding simplicity and generality.

In this paper, the standard form of a nonlinear optimization problem is used to obtain the optimal values of inner and outer phase shifts for different working points.

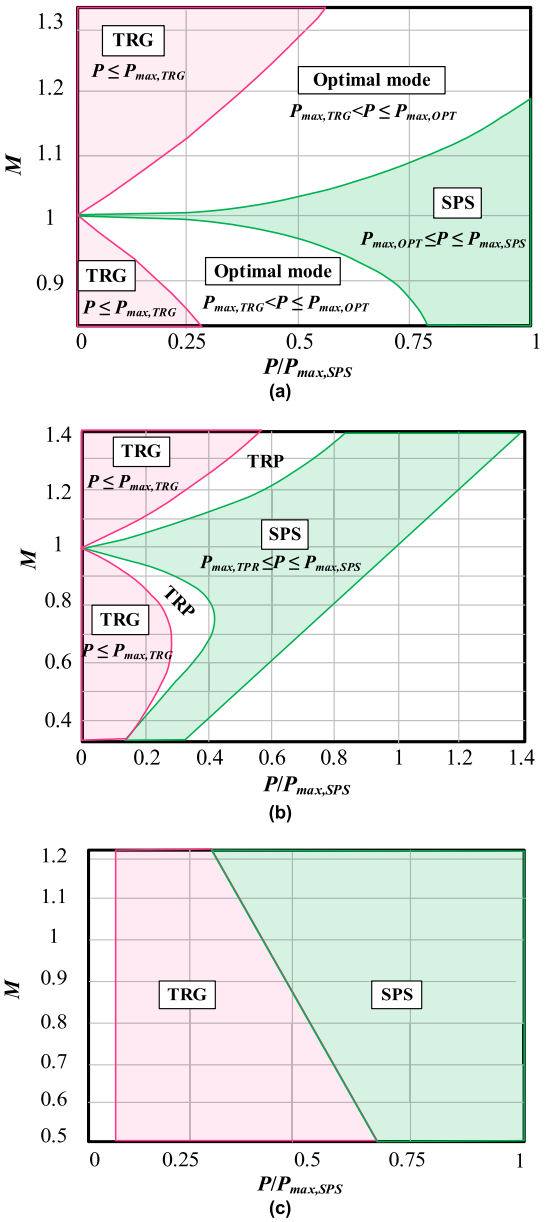

FIG. 12. **The control maps in the literature, (a) the DAB in [37]: $P = 2\,kW$, $240 < V_1 < 450$, $11 < V_2 < 16$, $N = 19$, (b) the DAB in [38]: $P = 1.5\,kW$, $240 < V_1 < 440$, $6 < V_2 < 16$, $N = 24$, (c) the DAB in [34]: $P = 1.2\,kW$, $28 < V_1 < 45$, $300 < V_2 < 400$, $1/N = 12$.**

In general, a standard nonlinear optimization problem can be expressed as:

$$\min f(x) \;\; such\ that \begin{cases} c(x) \le 0 \\ c_{eq}(x) = 0 \\ A.x \le b \\ A_{eq}.x = b_{eq} \\ Lb \le x \le Ub \end{cases} \tag{37}$$

The equality and inequality constraints in the optimization are specified by A_{eq}, b_{eq}, c_{eq}, and A, b, c matrices in (37), respectively. In addition, Lb and Ub are two vectors that

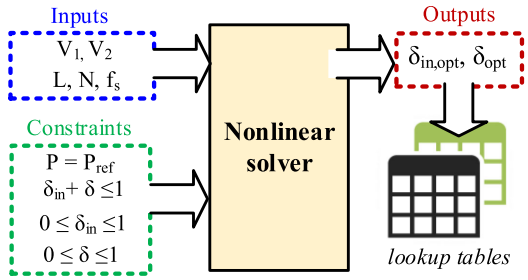

FIG. 13. **The inputs and the constraints in the proposed optimization approach.**

determine the low and upper boundaries of x. To associate (37) to the EPS and DPS modulation, x is defined as:

$$x = [x_1\ x_2]^T = [\delta_{in}\ \ \delta]^T \tag{38}$$

Depending on the objective and the modulation, $f(x)$ and the constraints are determined using Table I. The optimization process is explained in the following subsection.

A. OPTIMIZATION IN THE EPS MODULATION

The optimization targets in the EPS modulation can be either I_p or BFP minimization. The target function associated with I_p minimization can be defined as:

$$f_1(\delta_{in}, \delta) = \begin{cases} V_1(1-\delta_{in}) - NV_2(1-2\delta-2\delta_{in}), & NV_2 \le V_1 \\ NV_2(1-\delta_{in}) - V_1(1-2\delta-2\delta_{in}), & NV_2 > V_1 \end{cases} \tag{39}$$

Similarly, the second target function to minimize BFP can be expressed as:

$$f_2(\delta_{in}, \delta) = \begin{cases} \frac{[k(1-\delta_{in})+(2\delta-1)]^2}{2(k+1)}, & NV_2 \le V_1 \\ \frac{[M(1-\delta_{in})+(2\delta-1)]^2}{2(M+1)}, & NV_2 > V_1 \end{cases} \tag{40}$$

Therefore, $f(x)$ in (37) can be set as either f_1 or f_2 defined in (39), (40).

The optimization problem is solved for a specified power level called P_{ref}. Assuming $P_{ref} > 0$, the EPS constraints can be written as:

$$\begin{cases} P_{ref}/P_{max} = 2\delta_{in}(1-2\delta-\delta_{in}) + 4\delta(\delta-1) \\ \delta + \delta_{in} \le 1, \;\; 0 \le \delta \le 1, \;\; 0 \le \delta_{in} \le 1 \end{cases} \tag{41}$$

Using (41) and (37), (38), it can be concluded that:

$$\begin{cases} C_{eq}(x) = P_{ref}/P_{max} - 2x_1(1-2x_2-x_1) + 4x_2(x_{21}-1) \\ C,\ A_{eq}, b_{eq}, Lb = 0, \;\; Ub = 1, \;\; A = [1\ \ 1], \;\; b = 1 \end{cases} \tag{42}$$

Therefore, a standard nonlinear optimization problem related to the EPS modulation is defined. This problem can be solved by the *fmincon* function in MATLAB. A visual description of the optimization process is displayed in Fig. 13.

B. OPTIMIZATION IN THE DPS MODULATION

In the DPS modulation, either I_p or BFP can be set as the target function, similar to that explained in the case of the EPS. The target function associated with I_p minimization can be defined as:

$$f_1(\delta_{in}, \delta) = \begin{cases} V_1(1-\delta_{in}) - NV_2(1-2\delta-\delta_{in}), & NV_2 \le V_1 \\ NV_2(1-\delta_{in}) - V_1(1-2\delta-\delta_{in}), & NV_2 > V_1 \end{cases} \tag{43}$$

Similarly, the target function associated with BFP minimization is written as:

$$f_2(\delta_{in}, \delta) = \begin{cases} \frac{[k(1-\delta_{in})+(2\delta-1-\delta_{in})]^2}{2(k+1)}, & NV_2 \le V_1 \\ \frac{[M(1-\delta_{in})+(2\delta-1-\delta_{in})]^2}{2(M+1)}, & NV_2 > V_1 \end{cases} \tag{44}$$

The power equality constraint in the DPS modulation can be expressed $P = P_{ref}$, where:

$$P_{ref}/P_{max} = \begin{cases} -2\delta_{in}^2 + 4\delta(1-\delta), & \delta \ge \delta_{in} \\ \delta[4-4\delta_{in}-2\delta], & \delta < \delta_{in} \end{cases} \tag{45}$$

The equation in (45) should be rewritten in a suitable form for the nonlinear in MATLAB, then:

$$\frac{P_{ref}}{P_{max}} = u(\delta-\delta_{in})\left[-2\delta_{in}^2 + 4\delta(1-\delta)\right] + u(\delta_{in}-\delta)\,\delta[4-4\delta_{in}-2\delta] \tag{46}$$

Therefore:

$$C_{eq}(x) = \frac{P_{ref}}{P_{max}} - u(x_2-x_1)\left[-2x_1^2 + 4x_2(1-x_2)\right] - u(x_1-x_2)\,x_2[4-4x_1-2x_2] \tag{47}$$

Where $u(x)$ is a unit step function. Assuming $P_{ref} > 0$, the other constraints in DPS are:

$$\delta + \delta_{in} < 1,\ 0 \le \delta \le 1,\ \ 0 \le \delta_{in} \le 1 \tag{48}$$

Then:

$$Lb = 0,\ \ Ub = 1,\ \ A = [1\ \ 1],\ \ b = 1 \tag{49}$$

By specifying the target function and equality and inequality vectors associated with DPS method, this problem can be solved through standard nonlinear solvers.

C. THE UTILIZATION OF THE PROPOSED OPTIMIZATION APPROACH

A DAB converter has a continuous operating span. For example, in this study, a 10 kW DAB is designed as a part of an electric vehicle charging station with a voltage range of $700 < V_1 < 800$ and $380 < V_2 < 500$. The converter is also supposed to operate at low power ratios (at least one-third of the nominal power) with acceptable performance. However, the proposed optimization approach is designed to run offline using the voltages and the power value for a single operating point. Therefore, several runs are required to cover the entire working span by providing the optimal parameters.

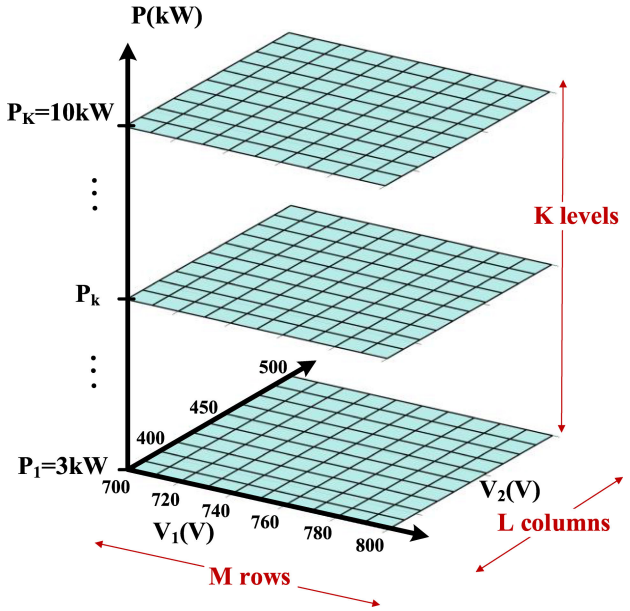

FIG. 14. Working span division into K levels and $M \times L$ number of segments on each level.

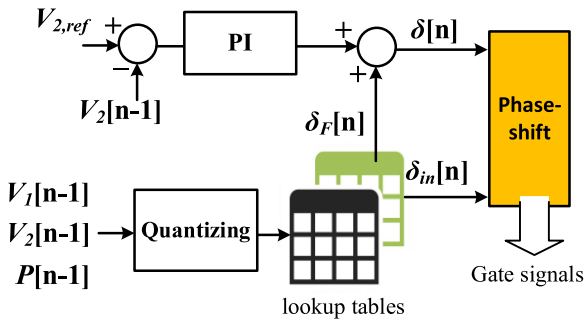

FIG. 15. The main controller in the designed DAB converter employing optimal values of inner and outer shifts.

Fig. 14 describes how the operating span in this DAB converter is divided into K power levels and $M \times L$ number of segments on the voltage planes, (V_1, V_2), at each power level. M and L are the number of rows and columns for the input and output voltages respectively. In addition, the power range quantization starts from 3 kW and ends at 10 kW. In this research, the offline optimization is run for the segments' central points, and the results are saved in K tables. Each table embeds the optimal parameters for a specified power level. The number of segments and power levels is selected so that the difference of the optimal parameters in two horizontally or vertically adjacent segments is slight. A larger number of segments or levels results in higher accuracy. However, a large lookup table occupies a vast memory area of the processor.

A PI controller is commonly used in a DAB converter's control to regulate the output voltage. As shown in Fig. 15, a closed-loop voltage controller is also employed in this study. Additionally, Fig. 15 demonstrates how the lookup tables are

TABLE IV The Simulated DAB Specification

Input voltage (V)	Output voltage (V)	Nominal power (kW)	f_s (kHz)	N	L (μH)	C (μF)
700-800	380-500	10	100	1.6	35	250

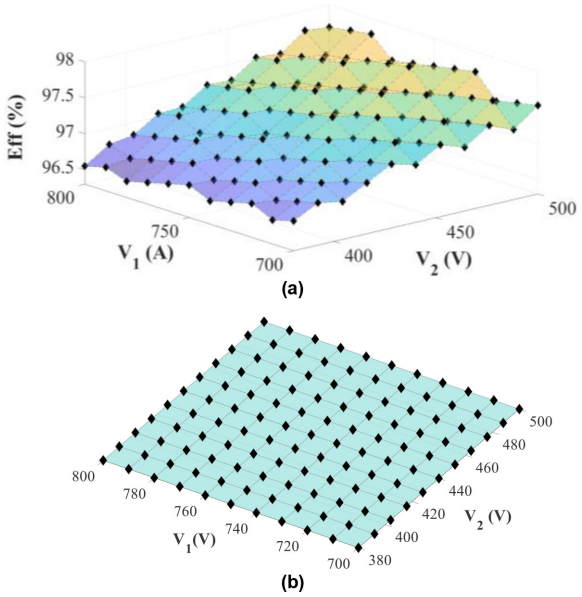

FIG. 16. The efficiency in the SPS modulation at the nominal power, $10\,kW$ (a) the efficiency curve of the SPS-controlled DAB, (b) the selected test points from the voltage range.

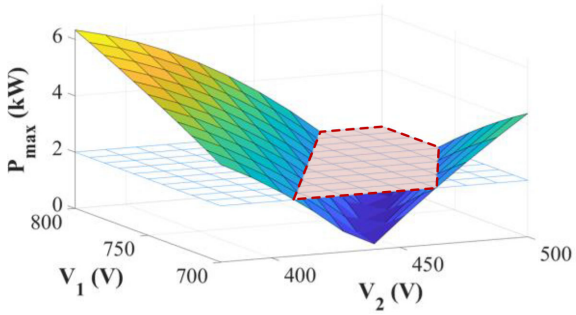

FIG. 17. The maximum TRG power in the voltage range. For $P = 2\,kW$, 40% of the voltage range is not covered by TRG; this area is surrounded with the dashed lines as an example.

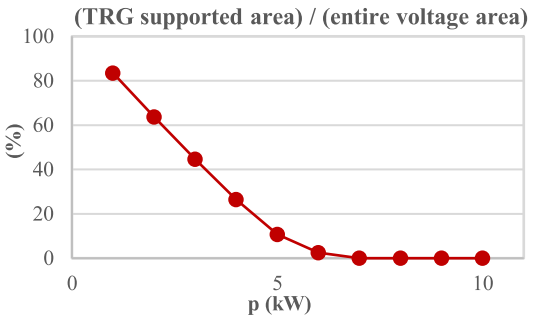

FIG. 18. The relative value of the TRG manageable area to the entire voltage range in the designed DAB converter.

utilized in the converter's control in practice. The measured voltages, as well as the instantaneous power value, are mapped into the nearest segment. Then, the optimal phase shift parameters are extracted from the specified lookup table. As shown in Fig. 15, the inner phase shift is used directly in the phase-shifter block. However, the outer phase shift is employed as a feed-forward input to accelerate the control process. The PI controller compensates for the slight difference between the optimal outer phase shift extracted from the table (called δ_F in Fig. 15) and the required δ for the voltage regulation.

V. COMPARISON OF THE MODULATION TECHNIQUES

As mentioned, a DAB converter is designed to be utilized in an "electric vehicle charging station," where the DAB input is connected to the output terminals of a three-phase rectifier [72]. The specification of the simulated system is summarized in Table IV. An ideal transformer in series with the inductor, L , connects the two bridges. The SiC-type switches, $1.2kV$, $55A$, $40\,m\Omega$ with the part number of SCT3040KR are employed in the bridges.

The DAB performance factors, including the efficiency, BFP, and I_p, are not constant during the entire voltage range. For instance, the efficiency curve for SPS at $P = 10$ kW is depicted in Fig. 16(a). The minimum and the maximum efficiencies are 96.5% and 97.7%, respectively. The average of the curve is used as a measure to represent the efficiency at $P = 10$ kW. Fig. 16(b) illustrates the simulated points from the voltage range. The average efficiency of these points is equal to 97.2%. A similar averaging process performed for all modulation techniques at the specified power levels, leading to a fair comparison among these modulations.

TRG only supports the low power levels; therefore, this method should be combined with other modulation techniques to guarantee the full power range operation. Fig. 17 displays the maximum power supported by TRG in the converter's voltage range. As an example, the non-supported voltage area at $P = 2$ kW is highlighted by the surrounding dashed line in Fig. 17. TRG covers only 60% of the voltage range at $P = 2$ kW; therefore, the rest 40% should be handled by other modulation techniques. The ratio of the TRG manageable area to the entire voltage range for different power levels is illustrated in Fig. 18. As it is mentioned, the vicinity of the central line is not covered by TRG, even at small loads. More than 80% of the voltage plane can be handled by TRG for the $P = 1$ kW. This ratio declines to zero at $P = 6$ kW.

Fig. 19(a)–(c) shows the results from the simulation of MTRG and two combinational modulation, namely TRG _TRP and TRG_SPS. In both combinational methods, TRG

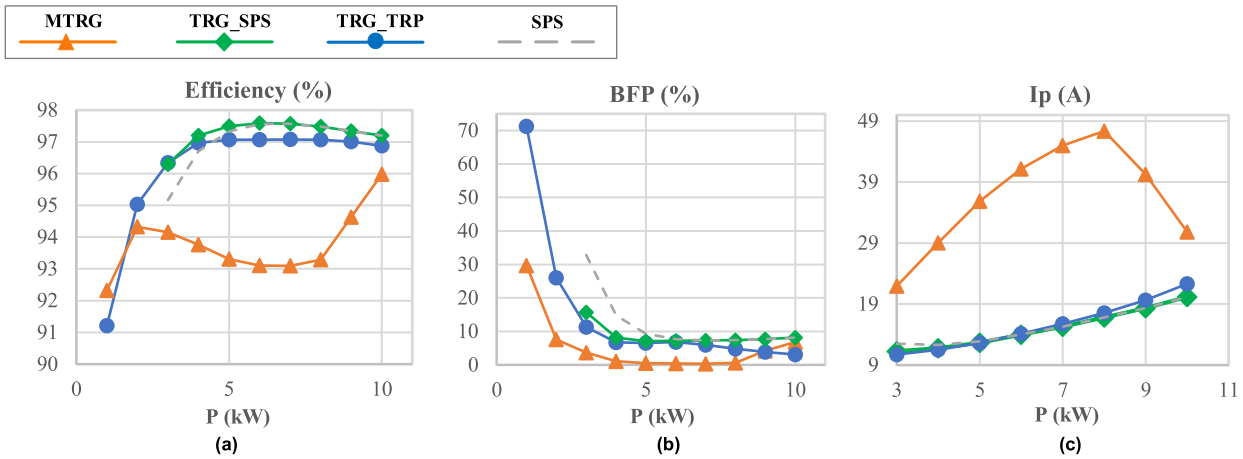

FIG. 19. The simulation results of the DAB converter, controlled by MTRG and the combinational method, including TRG_SPS and TRG_TRP (a) the efficiency, (b) the BFP, (c) the peak current.

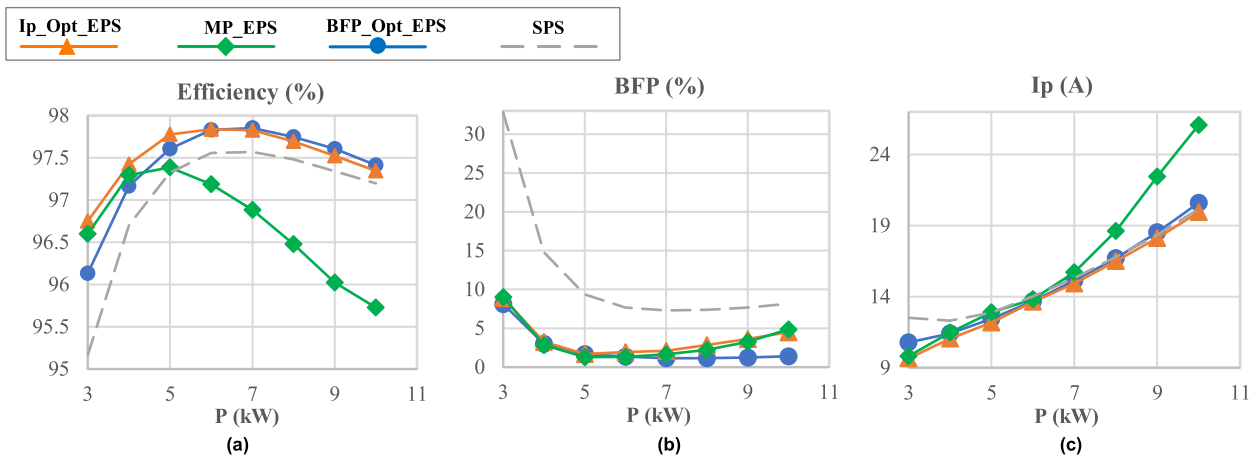

FIG. 20. The simulation results using the proposed optimization in the "EPS" modulation. (a) the efficiency, (b) the BFP, (c) the peak current. The EPS variants accompanied by BFP and I_p optimization are called BFP_Opt_EPS and Ip_Opt_EPS, respectively. The MP_EPS modulation represents the maximum power EPS method in [16].

is applied in its entire feasible region ($P < P_{max,\ TRG}$), defined in (30). At low power levels, such as $P = 3$ kW, TRG takes part more than 80% of the voltage range, considering Fig. 18. However, TRG does not support any single point of the voltage range for $P > 7$ kW. Therefore, in TRG_SPS and TRG_TRP, the full voltage range at high power values are exclusively covered by SPS and TRP, respectively.

MTRG supports the full operating range, but it produces acceptable outcomes, solely around 1 kW. It is worth considering, TRG_SPS fails to work properly for the powers less than 3 kW. As discussed in the design procedure of a DAB converter, δ cannot be set to minimal values. In overall, TRG_SPS achieves better outputs compared to TRP_TRG, regarding the higher efficiency. However, with respect to I_p and BFP, the two methods attain similar results. In summary, MTRG widens the power range of the converter; however, its performance is defeated by the traditional TRG. This research confirms SPS superiority compared to TRP in MOSFET switches, similar to the conclusion in [35].

The proposed optimization approach is applied in the designed converter. The two different target functions, including I_p and BFP, are investigated in this study. Figs. 20 and 21 demonstrates the results of employing the optimal parameters in the converter control using the EPS and DPS modulations. The modulation variants accompanied by optimization of I_p and BFP are called Ip_Opt and BFP_Opt in Figs. 20 and 21. The results of the EPS-based modulation (MP_EPS) in [16] are also added to Figs. 20 and 21.

As shown in Fig. 20(a), notably, Ip_Opt_EPS and BFP_Opt_EPS outperform SPS by more than 1% efficiency improvement in medium and small loads. The results prove that considering either optimization objectives in the EPS modulation achieves better performance for the DAB converter. In the non-optimized EPS, MP_EPS, the efficiency

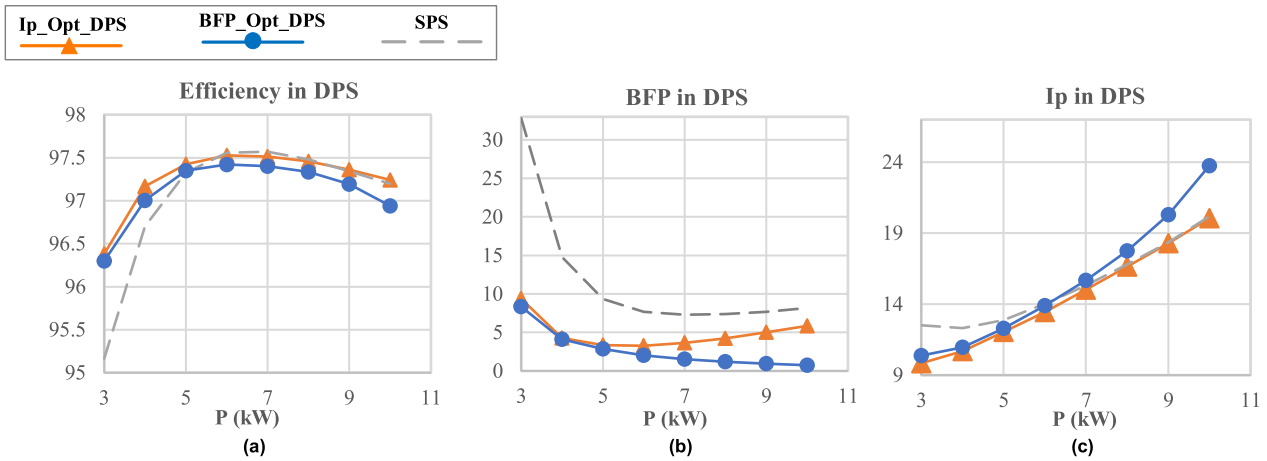

FIG. 21. The simulation results using the proposed optimization in the "DPS" modulation. (a) the efficiency, (b) the BFP, (c) the peak current. The DPS variants accompanied by BFP and I_p optimization are called BFP_Opt_DPS and Ip_Opt_DPS, respectively.

declines rapidly for $P > 5$ kW, showing the weakness of this method. The BFP ratio in the EPS variants and SPS depicted in Fig. 20(b) confirms a significant reduction of BFP using all the EPS-based. The results concerning the current stress are also shown in Fig. 20(c). EPS_Ip_Opt and EPS_MP have the lowest and highest current stress.

The same factors are examined in the DAB using the DPS modulation. The simulation results are shown in Fig. 21(a)–(c). The outperformance of DPS compared to SPS is limited to the power less than 5 kW. The efficiency increase using DPS is equal to 1% at 3 kW. Despite the reduction of I_p and BPF in the optimized DPS approaches, the efficiency is decreased in higher levels. The SPS and DPS efficiency curves intersect at $P = 5$ kW. The results demonstrate that generally EPS works better than SPS and DPS.

VI. CONCLUSION

In this study, the performance of different modulation techniques is evaluated in terms of efficiency, BFP, and current stress over the DAB's operating range. This comparison provides a guide to select the correct modulation at a specified power level acquiring the converter's highest performance at all the time.

The proposed optimization approach can help to enhance the performance of the EPS and DPS modulation techniques. Compared to SPS, the optimized EPS provides the inverter with a nearly 0.5%–1.5% efficiency increase considering the entire power range. Specifically, the improvement at low and medium power ratios is remarkable. MP_EPS functions similarly to the optimized EPS at low power ratios ($P < 5$ kW). However, MP_EPS performance for $P > 5kW$ is not satisfying. The optimized DPS improves the converter's efficiency by an average of 0.6% for $P < 4$ kW. Shortly, the optimized EPS excels in terms of the total performance compared to the optimized DPS.

MTRG widens the converter's operating power to lower power ratios. However, the performance of MTRG decreases intensely for $P > 1.5\,kW$ compared to the traditional TRG. The combination of TRG and TRP (TRG_TRP) covers a broader power range than TRG_SPS due to the limitation for the minimum value of δ in SPS. However, the combination of SPS and TRG excels in the medium and high-power ratios compared to TRG_TRP.

REFERENCES

[1] F. Krismer and J. W. Kolar, "Efficiency-optimized high-current dual active bridge converter for automotive applications," *IEEE Trans. Ind. Electron.*, vol. 59, no. 7, pp. 2745–2760, Jul. 2012, doi: 10.1109/TIE.2011.2112312.

[2] Y. Yan, H. Bai, A. Foote, and W. Wang, "Securing full-power-range zero-voltage switching in both steady-state and transient operations for a dual-active-bridge-based bidirectional electric vehicle charger," *IEEE Trans. Power Electron.*, vol. 7, no. 35, pp. 7506–7519, Jul. 2020, doi: 10.1109/TPEL.2019.2955896.

[3] L. Xue, Z. Shen, D. Boroyevich, P. Mattavelli, and D. Diaz, "Dual active bridge-based battery charger for plug-in hybrid electric vehicle with charging current containing low frequency ripple," *IEEE Trans. Power Electron.*, vol. 30, no. 12, pp. 7299–7307, Dec. 2015, doi: 10.1109/TPEL.2015.2413815.

[4] R. T. Naayagi, A. J. Forsyth, and R. Shuttleworth, "High-power bidirectional DC–DC converter for aerospace applications," *IEEE Trans. Power Electron.*, vol. 27, no. 11, pp. 4366–4379, Nov. 2012, doi: 10.1109/TPEL.2012.2184771.

[5] H. Tao, A. Kotsopoulos, J. L. Duarte, and M. A. M. Hendrix, "Transformer-coupled multiport ZVS bidirectional DC–DC converter with wide input range," *IEEE Trans. Power Electron.*, vol. 23, no. 2, pp. 771–781, Mar. 2008, doi: 10.1109/TPEL.2007.

[6] Y. Shi, R. Li, Y. Xue, and H. Li, "Optimized operation of current-fed dual active bridge DC–DC converter for PV applications," *IEEE Trans. Ind. Electron.*, vol. 62, no. 11, pp. 6986–6995, Nov. 2015, doi: 10.1109/TIE.2015.2432093.

[7] T. Zhao, G. Wang, S. Bhattacharya, and A. Q. Huang, "Voltage and power balance control for a cascaded H-Bridge converter-based solid-state transformer," *IEEE Trans. Power Electron.*, vol. 28, no. 4, pp. 1523–1532, Apr. 2013, doi: 10.1109/TPEL.2012.2216549.

[8] F. An, W. Song, K. Yang, S. Luo, and X. Feng, "Optimised power control and balance scheme for the output parallel dual-active-bridge DC-DC converters in power electronic traction transformer," *IET Power Electron.*, vol. 12, no. 9, pp. 2295–2303, Aug. 2019, doi: 10.1049/iet-pel.2018.5056.

[9] M. Rolak, C. Sobol, M. Malinowski, and S. Stynski, "Efficiency optimization of two dual active bridge converters operating in parallel," *IEEE Trans. Power Electron.*, vol. 35, no. 6, pp. 6523–6532, Jun. 2020, doi: 10.1109/TPEL.2019.2951833.

[10] H. Qin, and J. W. Kimball, "Generalized average modeling of dual active bridge DC–DC converter," *IEEE Trans. Power Electron.*, vol. 27, no. 4, pp. 2078–2084, Apr. 2012, doi: 10.1109/TPEL.2011.2165734.

[11] Y. Wang, S. W. H. de Haan, and J. A. Ferreira, "Optimal operating ranges of three modulation methods in dual active bridge converters," in *Proc. IEEE 6th Int. Power Electron. Motion Control Conf.*, 2009, pp. 1397–1401, doi: 10.1109/IPEMC.2009.5157602.

[12] G. G. Oggier, G. O. GarcÍa, and A. R. Oliva, "Switching control strategy to minimize dual active bridge converter losses," *IEEE Trans. Power Electron.*, vol. 24, no. 7, pp. 1826–1838, Jul. 2009, doi: 10.1109/TPEL.2009.2020902.

[13] G. Oggier, G. O. García, and A. R. Oliva, "Modulation strategy to operate the dual active bridge DC-DC converter under soft switching in the whole operating range," *IEEE Trans. Power Electron.*, vol. 26, no. 4, pp. 1228–1236, Apr. 2011, doi: 10.1109/TPEL.2010.2072966.

[14] A. K. Jain, and R. Ayyanar, "PWM control of dual active bridge: Comprehensive analysis and experimental verification," *IEEE Trans. Power Electron.*, vol. 26, no. 4, pp. 1215–1227, Apr. 2011, doi: 10.1109/TPEL.2010.2070519.

[15] W. Choi, K. Rho, and B. Cho, "Fundamental duty modulation of dual-active-bridge converter for wide-range operation," *IEEE Trans. Power Electron.*, vol. 31, no. 6, pp. 4048–4064, Jun. 2016, doi: 10.1109/TPEL.2015.2474135.

[16] B. Zhao, Q. Yu, and W. Sun, "Extended-phase-shift control of isolated bidirectional DC–DC converter for power distribution in microgrid," *IEEE Trans. Power Electron.*, vol. 27, no. 11, pp. 4667–4680, Nov. 2012, doi: 10.1109/TPEL.2011.2180928.

[17] N. Hou, W. Song, Y. Zhu, X. Sun, and W. Li, "Dynamic and static performance optimization of dual active bridge DC-DC converters," *J. Modern Power Syst. Clean Energy*, vol. 6, no. 3, pp. 607–618, May 2018.

[18] R. T. Naayagi, A. J. Forsyth, and R. Shuttleworth, "Performance analysis of extended phase-shift control of DAB DC-DC converter for aerospace energy storage system," in *Proc. IEEE 11th Int. Conf. Power Electron. Drive Syst.*, 2015, pp. 514–517, doi: 10.1109/PEDS.2015.7203567.

[19] M. Zheng, H. Wen, H. Shi, Y. Hu, Y. Yang, and Y. Wang, "Open-circuit fault diagnosis of dual active bridge DC-DC converter with extended-phase-shift control," *IEEE Access*, vol. 7, pp. 23752–23765, 2019, doi: 10.1109/ACCESS.2019.2899133.

[20] N. Hou, W. Song, and M. Wu, "Minimum-current-stress scheme of dual active bridge DC–DC converter with unified phase-shift control," *IEEE Trans. Power Electron.*, vol. 31, no. 12, pp. 8552–8561, Dec. 2016, doi: 10.1109/TPEL.2016.2521410.

[21] H. Shi *et al.*, "Minimum-backflow-power scheme of DAB-based solid-state transformer with extended-phase-shift control," *IEEE Trans. Ind. Appl.*, vol. 54, no. 4, pp. 3483–3496, Jul./Aug. 2018, doi: 10.1109/TIA.2018.2819120.

[22] H. Bai, and C. Mi, "Eliminate reactive power and increase system efficiency of isolated bidirectional dual-active-bridge DC–DC converters using novel dual-phase-shift control," *IEEE Trans. Power Electron.*, vol. 23, no. 6, pp. 2905–2914, Nov. 2008, doi: 10.1109/TPEL.2008.2005103.

[23] H. Bai, Z. Nie, and C. C. Mi, "Experimental comparison of traditional phase-shift, dual-phase-shift, and model-based control of isolated bidirectional DC–DC converters," *IEEE Trans. Power Electron.*, vol. 25, no. 6, pp. 1444–1449, Jun. 2010, doi: 10.1109/TPEL.2009.2039648.

[24] M. Tsai, C. Chu, and C. Chin, "Design a dual active bridge converter with symmetrical dual phase-shift strategy," in *Proc. IEEE Int. Conf. Appl. System Invention (ICASI)*, 2018, pp. 1002–1005, doi: 10.1109/ICASI.2018.8394442..

[25] B. Zhao, Q. Song, and W. Liu, "Power characterization of isolated bidirectional dual-active-bridge DC–DC converter with dual-phase-shift control," *IEEE Trans. Power Electron.*, vol. 27, no. 9, pp. 4172–4176, Sept. 2012, doi: 10.1109/TPEL.2012.2189586.

[26] B. Feng, Y. Wang, and J. Man, "A novel dual-phase-shift control strategy for dual-active-bridge DC-DC converter," in *Proc. IECON - 40th Annu. Conf. IEEE Ind. Electron. Soc.*, 2014, pp. 4140–4145, doi: 10.1109/IECON.2014.70491.

[27] V. Karthikeyan, and R. Gupta, "Closed-loop control of isolated dual active bridge converter using dual phase shift modulation," in *Proc. IECON- 41st Annu. Conf. IEEE Ind. Electron. Soc.*, 2015, pp. 2800–2805, doi: 10.1109/IECON.2015.7392526.

[28] K. Wu, C. W. de Silva, and W. G. Dunford, "Stability analysis of isolated bidirectional dual active full-bridge DC–DC converter with triple phase-shift control," *IEEE Trans. Power Electron.*, vol. 27, no. 4, pp. 2007–2017, Apr. 2012, doi: 10.1109/TPEL.2011.2167243.

[29] A. K. Bhattacharjee, and I. Batarseh, "Optimum hybrid modulation for improvement of efficiency over wide operating range for triple-phase-shift dual-active-bridge converter," *IEEE Trans. Power Electron.*, vol. 35, no. 5, pp. 4804–4818, May 2020, doi: 10.1109/TPEL.2019.2943392.

[30] J. Huang, Y. Wang, Z. Li, and W. Lei, "Unified triple-phase-shift control to minimize current stress and achieve full soft-switching of isolated bidirectional DC–DC converter," *IEEE Trans. Ind. Electron.*, vol. 63, no. 7, pp. 4169–4179, Jul. 2016, doi: 10.1109/TIE.2016.2543182.

[31] F. Xiong, J. Wu, and L. Hao, and Z. Liu, "Backflow power optimization control for dual active bridge DC-DC converters," *Energies*, vol. 10, pp. 1403, Sep. 2017.

[32] N. Schibli, "*Symmetrical Multilevel Converters With Two Quadrant DC/DC Feeding*," Ph.D. dissertation, Inst. Elect. Eng., The Ecole polytechnique fédérale de Lausanne (EPFL), Lausanne, Switzerland, 2000.

[33] F. Krismer, "Modeling and optimization of bidirectional dual active bridge DC/DC converter topologies," Ph.D. dissertation, Dept. Inf. Technol. Elect. Eng., ETH Zürich, Zürich, Switzerland, 2010.

[34] H. Zhou, and A. M. Khambadkone, "Hybrid modulation for dual-active-bridge bidirectional converter with extended power range for ultracapacitor application," *IEEE Trans. Ind. Appl.*, vol. 45, no. 4, pp. 1434–1442, Jul./Aug. 2009, doi: 10.1109/TIA.2009.2023493.

[35] V. Steub, "Study of modulation schemes for the dual-active-bridge converter in a grid-connected photovoltaic park," Master's thesis, Dept. Elect. Eng., Gothenburg, Sweden, 2018.

[36] G. Xu, D. Sha, J. Zhang, and X. Liao, "Unified boundary trapezoidal modulation control utilizing fixed duty cycle compensation and magnetizing current design for dual active bridge DC–DC converter," *IEEE Trans. Power Electron.*, vol. 32, no. 3, pp. 2243–2252, Mar. 2017, doi: 10.1109/TPEL.2016.2555328.

[37] F. Krismer, and J. W. Kolar, "Closed form solution for minimum conduction loss modulation of DAB converters," *IEEE Trans. Power Electron.*, vol. 27 no. 1, pp. 174–188, Jan. 2012, doi: 10.1109/TPEL.2011.2157976,.

[38] Y. Cui, R. Hou, P. Malysz, and A. Emadi, "Improved combined modulation strategy for dual active bridge converter in electrified vehicles," in *Proc. IEEE Transp. Electrific. Conf. Expo (ITEC)*, 2017, pp. 101–107, doi: 10.1109/ITEC.2017.7993254.

[39] B. Zhao, Q. Song, W. Liu, and Y. Sun, "Overview of dual-active-bridge isolated bidirectional DC–DC converter for high-frequency-link power-conversion system," *IEEE Trans. Power Electron.*, vol. 29, no. 8, pp. 4091–4106, Aug. 2014, doi: 10.1109/TPEL.2013.2289913.

[40] N. Hou, and Y. W. Li, "Overview and comparison of modulation and control strategies for a nonresonant single-phase dual-active-bridge DC–DC converter," *IEEE Trans. Power Electron.*, vol. 35, no. 3, pp. 3148–3172, Mar. 2020, doi: 10.1109/TPEL.2019.2927930.

[41] A. Rodríguez, A. Vázquez, D. G. Lamar, M. M. Hernando, and J. Sebastián, "Different purpose design strategies and techniques to improve the performance of a dual active bridge with phase-shift control," *IEEE Trans. Power Electron.*, vol. 30, no. 2, pp. 790–804, Feb. 2015, doi: 10.1109/TPEL.2014.2309853.

[42] M. N. Kheraluwala, R. W. Gascoigne, D. M. Divan, and E. D. Baumann, "Performance characterization of a high-power dual active bridge DC-to-DC converter," *IEEE Trans. Ind. Appl.*, vol. 28, no. 6, pp. 1294–1301, Nov./Dec. 1992, doi: 10.1109/28.175280.

[43] D. Costinett, D. Maksimovic, and R. Zane, "Design and control for high efficiency in high step-down dual active bridge converters operating at high switching frequency," *IEEE Trans. Power Electron.*, vol. 28, no. 8, pp. 3931–3940, Aug. 2013, doi: 10.1109/TPEL. 2012.2228237.

[44] H. Akagi, T. Yamagishi, N. M. L. Tan, S. Kinouchi, Y. Miyazaki, and M. Koyama, "Power-loss breakdown of a 750-V 100-kW 20-kHz bidirectional isolated DC–DC converter using SiC-MOSFET/SBD dual modules," *IEEE Trans. Ind. Appl.*, vol. 51, no. 1, pp. 420–428, Jan./Feb. 2015, doi: 10.1109/TIA.2014.2331426.

[45] F. Krismer, and J. W. Kolar, "Accurate power loss model derivation of a high-current dual active bridge converter for an automotive application," *IEEE Trans. Ind. Electron.*, vol. 57, no. 3, pp. 881–891, Mar. 2010, doi: 10.1109/TIE.2009.

[46] D. Costinett, D. Maksimovic, and R. Zane, "Design and control for high efficiency in high step-down dual active bridge converters operating at high switching frequency," *IEEE Trans. Power Electron.*, vol. 28, no. 8, pp. 3931–3940, Aug. 2013, doi: 10.1109/TPEL.2012.2228237.

[47] G. Xu, Y. Xu, D. Sha, and X. Liao, "Fixed duty cycle compensation and magnetizing current design for DAB DC-DC converter with conventional trapezoidal modulation to achieve zero voltage switching," in *Proc. IEEE 8th Int. Power Electron. Motion Control Conf.*, 2016, pp. 433–438, doi: 10.1109/IPEMC.2016.7512325.

[48] N. M. L. Tan, T. Abe, and H. Akagi, "Experimental discussions on operating frequencies of a bidirectional isolated DC-DC converter for a battery energy storage system," in *Proc. IEEE Energy Convers. Congr. Expo.*, 2013, pp. 2333–2340, doi: 10.1109/ECCE.2013.6646999,.

[49] F. Krismer and J. W. Kolar, "Accurate small-signal model for the digital control of an automotive bidirectional dual active bridge," *IEEE Trans. Power Electron.*, vol. 24, no. 12, pp. 2756–2768, Dec. 2009, doi: 10.1109/TPEL.2009.2027904.

[50] S. S. Shah, and S. Bhattacharya, "A simple unified model for generic operation of dual active bridge converter," *IEEE Trans. Ind. Electron.*, vol. 66, no. 5, pp. 3486–3495, May 2019, doi: 10.1109/TIE.2018.2850012.

[51] J. A. Mueller, and J. W. Kimball, "An improved generalized average model of DC–DC dual active bridge converters," *IEEE Trans. Power Electron.*, vol. 33, no. 11, pp. 9975–9988, Nov. 2018, doi: 10.1109/TPEL.2018.2797966.

[52] X. Li and Y. Li, "An optimized phase-shift modulation for fast transient response in a dual-active-bridge converter," *IEEE Trans. Power Electron.*, vol. 29, no. 6, pp. 2661–2665, Jun. 2014, doi: 10.1109/TPEL.2013.2294714.

[53] S. Dutta, S. Hazra, and S. Bhattacharya, "A digital predictive current-mode controller for a single-phase high-frequency transformer-isolated dual-active bridge DC-to-DC converter," *IEEE Trans. Ind. Electron.*, vol. 63, no. 9, pp. 5943–5952, Sep. 2016, doi: 10.1109/TIE.2016.2551201.

[54] F. Xiong, J. Wu, Z. Liu, and L. Hao, "Current sensorless control for dual active bridge DC–DC converter with estimated load-current feedforward," *IEEE Trans. Power Electron.*, vol. 33, no. 4, pp. 3552–3566, Apr. 2018, doi: 10.1109/TPEL.2017.2.

[55] Y. Jeung and D. Lee, "Voltage and current regulations of bidirectional isolated dual-active-bridge DC–DC converters based on a double-integral sliding mode control," *IEEE Trans. Power Electron.*, vol. 34, no. 7, pp. 6937–6946, Jul. 2019, doi: 10.1109/TPEL.2018.2873834.

[56] Z. Shan, J. Jatskevich, H. H. Iu, and T. Fernando, "Simplified load-feedforward control design for dual-active-bridge converters with current-mode modulation," *IEEE J. Emerg. Sel. Topics Power Electron.*, vol. 6, no. 4, pp. 2073–2085, Dec. 2018, doi: 10.1109/JESTPE.2018.2797998.

[57] W. Song, N. Hou, and M. Wu, "Virtual direct power control scheme of dual active bridge DC–DC converters for fast dynamic response," *IEEE Trans. Power Electron.*, vol. 33, no. 2, pp. 1750–1759, Feb. 2018, doi: 10.1109/TPEL.2017.2682982.

[58] F. An, W. Song, and K. Yang, "Optimised power control with extended phase shift in dual-active-bridge dc–dc converters," *Electron. Lett.*, vol. 54, no. 10, pp. 651–653, May 2018, doi: 10.1049/el.2018.0683.

[59] H. Wen, W. Xiao, and B. Su, "Nonactive power loss minimization in a bidirectional isolated DC–DC converter for distributed power systems," *IEEE Trans. Ind. Electron.*, vol. 61, no. 12, pp. 6822–6831, Dec. 2014, doi: 10.1109/TIE.2014.2316229.

[60] H. Qin and J. W. Kimball, "Closed-loop control of DC–DC dual-active-bridge converters driving single-phase inverters," *IEEE Trans. Power Electron.*, vol. 29, no. 2, pp. 1006–1017, Feb. 2014, doi: 10.1109/TPEL.2013.2257859.

[61] S. Bal, D. B. Yelaverthi, A. K. Rathore, and D. Srinivasan, "Improved modulation strategy using dual phase shift modulation for active commutated current-fed dual active bridge," *IEEE Trans. Power Electron.*, vol. 33, no. 9, pp. 7359–7375, Sep. 2018, doi: 10.1109/TPEL.2017.2764917.

[62] B. Zhao, Q. Song, and W. Liu, "Efficiency characterization and optimization of isolated bidirectional DC–DC converter based on dual-phase-shift control for DC distribution application," *IEEE Trans. Power Electron.*, vol. 28, no. 4, pp. 1711–1727, Apr. 2013, doi: 10.1109/TPEL.2012.2210563.

[63] S. Chi, P. Liu, X. Li, M. Xu, and S. Li, "A novel dual phase shift modulation for dual-active-bridge converter," in *Proc. IEEE Energy Convers. Congr. Expo.*, 2019, pp. 1556–1561, doi: 10.1109/ECCE.2019.8912591.

[64] X. Liu *et al.*, "Novel dual-phase-shift control with bidirectional inner phase shifts for a dual-active-bridge converter having low surge current and stable power control," *IEEE Trans. Power Electron.*, vol. 32, no. 5, pp. 4095–4106, May 2017, doi: 10.1109/TPEL.2016.2593939.

[65] H. L. Chan, K. W. E. Cheng, and D. Sutanto, "An extended load range ZCS-ZVS bi-directional phase-shifted DC-DC converter," in *Proc. 8th Int. Conf. Power Electron. Variable Speed Drives*, 2000, pp. 74–79, doi: 10.1049/cp:20000223.

[66] S. S. Muthuraj, V. K. Kanakesh, P. Das, and S. K. Panda, "Triple phase shift control of an LLL tank based bidirectional dual active bridge converter," *IEEE Trans. Power Electron.*, vol. 32, no. 10, pp. 8035–8053, Oct. 2017, doi: 10.1109/TPEL.2016.2637506.

[67] A. Tong, L. Hang, G. Li, X. Jiang, and S. Gao, "Modeling and analysis of a dual-active-bridge-isolated bidirectional DC/DC converter to minimize RMS current with whole operating range," *IEEE Trans. Power Electron.*, vol. 33, no. 6, pp. 5302–5353, Jun. 2018, doi: 10.1109/TPEL.2017.2692276.

[68] J. Hiltunen, V. Väisänen, R. Juntunen, and P. Silventoinen, "Variable-frequency phase shift modulation of a dual sctive bridge converter," *IEEE Trans. Power Electron.*, vol. 30, no. 12, pp. 7138–7148, Dec. 2015, doi: 10.1109/TPEL.2015.2390913.

[69] Y. Cho, W. Cha, J. Kwon, and B. Kwon, "High-ffficiency bidirectional DAB inverter using a novel hybrid modulation for stand-alone power generating system with low input voltage," *IEEE Trans. Power Electron.*, vol. 31, no. 6, pp. 4138–4147, Jun. 2016, doi: 10.1109/TPEL.2015.2476336.

[70] J. Lu *et al.*, "Applying variable-switching-frequency variable-phase-shift control and E-mode GaN HEMTs to an indirect matrix converter-based EV battery charger," *IEEE Trans. Transp. Electrific.*, vol. 3, no. 3, pp. 554–564, Sep. 2017, doi: 10.1109/TTE.2017.2723944.

[71] G. G. Oggier and M. Ordonez, "High-efficiency DAB converter using switching sequences and burst mode," *IEEE Trans. Power Electron.*, vol. 31, no. 3, pp. 2069–2082, Mar. 2016, doi: 10.1109/TPEL.2015.2440753.

[72] H. Ramakrishnan, "Bi-Directional, dual active bridge reference design for level 3 electric vehicle charging stations," Systems engineer at Texas Instruments, India, Jun. 2019, https://www.ti.com/lit/ug/tidues0/tidues0.pdf?ts=1623573605532

N. NOROOZI (Member, IEEE) was born in Tabriz, Iran, in 1985. She received the B.S. degree in electrical engineering from the University of Tehran, Iran, in 2007, and the M.S. and Ph.D. degrees from the Sharif University of Technology, Tehran, Iran, in 2010 and 2018, respectively. She was the Chief Student Member of Electric Drive and Power Electronics Laboratory with the Sharif University of Technology. In 2019, she joined the McMaster Automotive Resource Centre, Hamilton, ON, Canada, as a Postdoctoral Fellow, focusing on electric vehicles. She is currently working on motor drivers in collaboration with the Department of Electrical and Computer Engineering at McMaster University, Hamilton, ON, Canada. She made contribution in publishing more than 20 papers covering a variety of fields in power electronics. Her main research interests include renewable energy, power converters, and motor usage in medical applications.

A. EMADI (Fellow, IEEE) received the B.S. and M.S. degrees in electrical engineering with highest distinction from the Sharif University of Technology, Tehran, Iran, in 1995 and 1997, respectively, and the Ph.D. degree in electrical engineering from Texas A&M University, College Station, TX, USA, in 2000. He is currently the Canada Excellence Research Chair Laureate of McMaster University, Hamilton, ON, Canada. He is also the holder of the NSERC/FCA Industrial Research Chair of electrified powertrains and Tier I Canada Research Chair of transportation electrification and smart mobility. Before joining McMaster University, he was the Harris Perlstein Endowed Chair Professor of engineering and Director of the Electric Power and Power Electronics Center and Grainger Laboratories, Illinois Institute of Technology, Chicago, IL, USA, where he established research and teaching facilities and courses in power electronics, motor drives, and vehicular power systems. He was the Founder, Chairman, and President of Hybrid Electric Vehicle Technologies, Inc., a university spin-off company of Illinois Tech. He is the President and Chief Executive Officer of Enedym Inc., Hamilton, ON, Canada and Menlolab Inc., Hamilton, ON, Canada, two McMaster University spin-off companies. He is the principal author or coauthor of more than 500 journal and conference papers and several books, including *Vehicular Electric Power Systems* (2003), *Energy Efficient Electric Motors* (2004), *Uninterruptible Power Supplies and Active Filters* (2004), *Modern Electric, Hybrid Electric, and Fuel Cell Vehicles* (2nd ed, 2009), and *Integrated Power Electronic Converters and Digital Control* (2009). He is also the Editor of the *Handbook of Automotive Power Electronics and Motor Drives* (2005) and *Advanced Electric Drive Vehicles* (2014). He is the co-editor of the *Switched Reluctance Motor Drives* (2018). He was the Inaugural General Chair of the 2012 IEEE Transportation Electrification Conference and Expo and has chaired several IEEE and SAE conferences in the areas of vehicle power and propulsion. From 2014 to 2020, he was the founding Editor-in-Chief of the IEEE TRANSACTIONS ON TRANSPORTATION ELECTRIFICATION.

M. NARIMANI (Senior Member, IEEE) received the Ph.D. degree in electrical engineering from the University of Western Ontario, London, ON, Canada, in 2012. He is currently an Assistant Professor with the Department of Electrical and Computer Engineering, McMaster University, Hamilton, ON, Canada. He is the Canada Research Chair of McMaster University. Prior joining McMaster University, he was a Power Electronics Engineer with Rockwell Automation Canada, Cambridge, ON, Canada. He has authored or coauthored more than 130 journal and conference proceeding papers, coauthored a Wiley-IEEE Press book, *High-Power Converters and AC Drives* (2017), and holds nine issued or pending US or European patents. His current research interests include power conversion, high-power converters, control of power electronics converters, fast EV Chargers, and wireless EV charging systems.